

Gravitational Collapse in Turbulent Molecular Clouds. I. Gasdynamical Turbulence.

Ralf S. Klessen^{1,2}

Fabian Heitsch²

Mordecai-Mark Mac Low^{2,3}

(accepted to *The Astrophysical Journal*)

ABSTRACT

Observed molecular clouds often appear to have very low star formation efficiencies and lifetimes an order of magnitude longer than their free-fall times. Their support is attributed to the random supersonic motions observed in them. We study the support of molecular clouds against gravitational collapse by supersonic, gas dynamical turbulence using direct numerical simulation. Computations with two different algorithms are compared: a particle-based, Lagrangian method (SPH), and a grid-based, Eulerian, second-order method (ZEUS). The effects of both algorithm and resolution can be studied with this method. We find that, under typical molecular cloud conditions, global collapse can indeed be prevented, but density enhancements caused by strong shocks nevertheless become gravitationally unstable and collapse into dense cores and, presumably, stars. The occurrence and efficiency of local collapse decreases as the driving wave length decreases and the driving strength increases. It appears that local collapse can only be prevented entirely with unrealistically short wave length driving, but observed core formation rates can be reproduced with more realistic driving. At high collapse rates, cores are formed on short time scales in coherent structures with high efficiency, while at low collapse rates they are scattered randomly throughout the region and exhibit considerable age spread. We suggest that this naturally explains the observed distinction between isolated and clustered star formation.

¹Sterrewacht Leiden, Postbus 9613, 2300-RA Leiden, The Netherlands; E-mail: klessen@strw.leidenuniv.nl

²Max-Planck-Institut für Astronomie, Königstuhl 17, D-69117 Heidelberg, Germany; E-mail: heitsch@mpia-hd.mpg.de

³Department of Astrophysics, American Museum of Natural History, Central Park West at 79th Street, New York, New York 10024-5192, USA; E-mail: mordecai@amnh.org

Subject headings: hydrodynamics — ISM: clouds — ISM: kinematics and dynamics — stars: formation — turbulence

1. Motivation

All presently known star formation occurs in cold molecular clouds. Application of the pioneering work of Jeans (1902) on the stability of self-gravitating gaseous systems shows that observed molecular clouds vastly exceed the critical mass for gravitational collapse. Thus, clouds should efficiently form stars on a free-fall time scale of the order of $\tau_{\text{ff}} \sim 10^6$ years in the absence of other effects. However, the lifetime of a typical molecular cloud is generally believed to be a factor of ten or twenty longer than predicted by Jeans’ classical theory (Blitz & Shu 1980), although we note that this is subject to controversy. Ballesteros-Paredes, Hartmann, & Vázquez-Semadeni (1999) and Elmegreen (2000) for example have argued that not only is the internal structure of molecular clouds transient, but that the clouds as a whole may be rather short-lived objects. They suggested that lifetimes of order of τ_{ff} may actually be necessary to explain the lack of 10 – 20 million year old T Tauri stars associated with some molecular clouds. It is observed that stars often do not form in one ‘catastrophic’ event associated with the global collapse of the entire cloud. Instead, they form in very localized regions dispersed through an *apparently* stable cloud (for an overview see Williams, Blitz & McKee 1999 and references therein). The total efficiency of conversion from gas into stars in typical molecular clouds is very low—of the order of a few percent (e.g. Duerr, Imhoff, & Lada 1982; Leisawitz, Bash, & Thaddeus 1989). A comprehensive astrophysical explanation remains elusive and its discovery remains one of the great challenges for any theory of star formation.

Molecular clouds are turbulent. This is an essential ingredient for understanding their properties and characteristic spatial and temporal behavior. Turbulent gas motions are highly supersonic as indicated by the superthermal line widths observed throughout molecular clouds (Williams et al. 1999). The kinetic energy carried in that motion is sufficient to balance the potential energy of the cloud, presumably halting global collapse, a proposition that we will test in this paper. However, it can be shown that interstellar turbulence decays quite rapidly, on time scales of the order of the free-fall time of the system

$$\tau_{\text{ff}} = \sqrt{\frac{3\pi}{32G\rho}} \quad (1)$$

(Mac Low et al. 1998, Stone, Ostriker & Gammie 1998, Mac Low 1999, see also Porter, Pouquet & Woodward 1992a,b, 1994 and Padoan & Nordlund 1999). Strictly speaking, equation 1 is only valid for spherical perturbations with homogeneous density ρ , with G denoting the gravitational constant. However, for more general geometries or density distributions equation 1 still gives a good approximation to τ_{ff} if we take ρ to be the *mean* density of the system. To explain their observed long life times, turbulence in molecular clouds must be constantly driven (Gammie & Ostriker 1996, Mac Low 1999). The interplay between self-gravity on the one hand (leading to local collapse and star formation) and turbulent gas motion on the other hand (trying to prevent this process) appears to play a key role in regulating the structure of molecular clouds and determining where and when stars form.

Unfortunately, a theory of compressible turbulence complete enough to fully address the issue of stability against gravitational collapse does not exist, nor is it even visible on the horizon. A variety of schemes have been proposed to incorporate the effect of incompressible turbulence into a gravitational stability analysis. However, molecular clouds are extremely compressible. Moreover, the approximations necessary for solution of the resulting equations are very stringent and appear to severely limit their applicability to the physical conditions found in interstellar clouds. This situation demands a thorough numerical approach. Although still far away from fully describing all phenomena present in molecular clouds, numerical modeling can capture the important features of supersonic, compressible turbulence in self-gravitating, ideal gases. In this paper, we perform a numerical Jeans analysis for self-gravitating, compressible, turbulent gas, and apply the result to molecular clouds and star forming regions. We do not include magnetic fields here, but the work presented here provides the foundation for studies including magnetic fields. Preliminary results appear not to reach markedly different conclusions (Mac Low, Klessen, & Heitsch 1999).

In § 2 we summarize previous work on the question of stability against collapse in self-gravitating turbulent media. Then in § 3 we describe our numerical schemes and models. The dynamical evolution of our models is discussed in § 4, which also introduces the concept of local versus global collapse. In § 5 we perform a Fourier analysis to quantify the collapse behavior on different spatial scales. Section 6 explores the implications of our results for star formation in molecular clouds. We speculate about the difference between the ‘clustered’ and ‘isolated’ modes of star formation and about the different time scales involved. Finally in § 7 we summarize our work.

2. Jeans Analysis

A first statement about cloud stability can be made from considering the virial theorem. Naïvely speaking, in equilibrium the total kinetic energy in the system adds up to half its potential energy, $E_{\text{kin}} + 1/2 E_{\text{pot}} = 0$. If $E_{\text{kin}} + 1/2 E_{\text{pot}} < 0$ the system collapses, while $E_{\text{kin}} + 1/2 E_{\text{pot}} > 0$ implies expansion. In turbulent clouds, the total kinetic energy includes not only the internal energy but also the contributions from turbulent gas motions. If this is taken into account, simple energy considerations can already provide a qualitative description of the collapse behavior of turbulent self-gravitating media (Bonazzola et al. 1987).

A more thorough investigation, however, requires a linear stability analysis. For the case of an isothermal, infinite, homogeneous, self-gravitating medium at rest (i.e. without turbulent motions) Jeans (1902) derived a relation between the oscillation frequency ω and the wave number k of small perturbations,

$$\omega^2 - c_s^2 k^2 + 4\pi G \rho_0 = 0, \quad (2)$$

where c_s is the isothermal sound speed, G the gravitational constant, and ρ_0 the initial mass

density. Note that the derivation includes the ad hoc assumption that the linearized version of the Poisson equation describes only the relation between the perturbed potential and the perturbed density, neglecting the potential of the homogeneous solution. This is the so-called ‘Jeans swindle’. The third term in equation 2 is responsible for the existence of decaying and growing modes, as pure sound waves stem from the dispersion relation $\omega^2 - c_s^2 k^2 = 0$. Perturbations are unstable against gravitational contraction if their wave number is below a critical value, the Jeans wave number k_J , i.e. if

$$k^2 < k_J^2 \equiv \frac{4\pi G \rho_0}{c_s^2}, \quad (3)$$

or equivalently if the wave length of the perturbation exceeds a critical size given by $\lambda_J \equiv 2\pi k_J^{-1}$. This directly translates into a mass limit. All perturbations with masses exceeding the Jeans mass,

$$M_J \equiv \rho_0 \lambda^3 = \left(\frac{\pi}{G}\right)^{3/2} \rho_0^{-1/2} c_s^3, \quad (4)$$

will collapse under their own weight. As we describe the dynamical evolution of cubic subregions inside molecular clouds, we use the cubic definition of the Jeans mass. The critical mass for spherical perturbations is lower by a factor of $\pi/6$.

Attempts to include the effect of turbulent motions into this analysis were already being made in the middle of the century by von Weizsäcker (1943, 1951), who also considered the production of interstellar clouds from the shocks and density fluctuations in compressible turbulence. A more quantitative theory was proposed by Chandrasekhar (1951), who studied the effect of microturbulence on gravitational collapse, assuming that collapse occurs on scales much greater than the outer scale of turbulence. He derived a dispersion relation similar to equation 2 replacing $c_s^2 \rightarrow c_s^2 + 1/3 \langle v^2 \rangle$, where $\langle v^2 \rangle$ is the overall velocity dispersion due to turbulent motions. Developments through the mid-eighties are reviewed by Scalo (1985). Particularly noteworthy is the work of Sasao (1973), who may have been the first to quantitatively show that the generation of density enhancements by turbulence, which Chandrasekhar (1951) neglected, might be as important as turbulent support. In a more recent analysis, Bonazzola et al. (1987) suggested a wave length dependent effective sound speed $c_s^2(k) = c_s^2 + 1/3 v^2(k)$, leading to a dispersion relation

$$\omega^2 - \left(c_s^2 + \frac{1}{3}v^2(k)\right) k^2 + 4\pi G \rho_0 = 0. \quad (5)$$

In this description, the stability of the system depends not only on the total amount of energy, but also on the wave length distribution of the energy, since $v^2(k)$ depends on the turbulent power spectrum $\epsilon(k)$ as

$$v^2(k) \equiv \int_k^\infty \epsilon(k') dk'. \quad (6)$$

Thus, the system can be stable at some wave lengths, but not at others. This approach was also adopted by Vázquez-Semadeni & Gazol (1995), who added Larson’s (1981) empirical scaling relations to the analysis.

The most elaborate investigation of the stability of turbulent, self-gravitating gas was made by Bonazzola et al. (1992), who used renormalization group theory to derive a dispersion relation with a generalized, wave number-dependent, effective sound speed and an effective kinetic viscosity that together account for turbulence at all wave lengths shorter than the one in question. They found a general dispersion relation (their equation 4.13) that, if applied to turbulence with a power-law energy spectrum $\epsilon(k) = Ak^{-\alpha}$, predicts a critical value of the power-law exponent $\alpha = 3$. According to their analysis, turbulence with a spectrum steeper than this can support a region against collapse at large scales, and below the thermal Jeans scale, but not in between. On the other hand, they claim that turbulence with a shallower slope, as is expected for incompressible turbulence (Kolmogorov 1941), Burgers turbulence (Lesieur 1997), or shock dominated flows (Passot, Pouquet & Woodward 1988), cannot support clouds against collapse at scales larger than the thermal Jeans wave length.

These analytical approaches make a strong assumption that substantially limits their reliability, namely that the equilibrium state is homogeneous, with constant density ρ_0 . However, observations clearly show that molecular clouds are extremely non-uniform. In fact, it may even be possible to describe the equilibrium state as an inherently inhomogeneous thermodynamic critical point (de Vega, Sánchez & Combes 1996a,b; de Vega & Sánchez 1999). As a consequence of the assumption of homogeneity, the further assumption of microturbulence must then be made. The largest turbulent scale is significantly smaller than the scale of the analysis. Interstellar turbulence, however, does not appear to exhibit such a cut-off in the power spectrum, but rather extends over *all* spatial scales present in the system. A further corollary of the assumption of homogeneity is that the turbulent dynamical time scale is much shorter than the collapse time scale τ_{ff} , which is only justified if the assumption of microturbulence holds.

One way to achieve progress and circumvent the restrictions of a purely analytical approach is to perform numerical simulations. Bonazzola et al. (1987), for example, used low resolution (32×32 collocation points) calculations with a 2-dimensional spectral code to support their analytical results. Also restricted to two dimensions were the hydrodynamical studies by Passot et al. (1988), Léorat, Passot & Pouquet (1990), Vázquez-Semadeni et al. (1995) and Ballesteros-Paredes, Vázquez-Semadeni & Scalo (1999), although performed with far higher resolution. Magnetic fields were introduced in two dimensions by Passot, Vázquez-Semadeni, & Pouquet (1995), and extended to three dimensions with self-gravity (though at only 64^3 resolution) by Vázquez-Semadeni, Passot, & Pouquet (1996). A careful analysis of 1-dimensional computations including both MHD and self-gravity was presented by Gammie & Ostriker (1996), who extended their work to 2.5 dimensions more recently (Ostriker, Gammie, & Stone 1999). Preliminary results of high-resolution (256^3 zone) simulations with MHD and self-gravity have been presented by Mac Low et al. (1999) and by Ostriker, Gammie, & Stone (1998). In the present paper we use two numerical algorithms to examine the stability properties of three-dimensional hydrodynamical turbulence at higher resolution than before. In subsequent work in preparation we will include magnetic fields as

well.

3. Numerical Methods

Direct numerical simulation of the Euler equations for gas flow does not reach the enormous Reynolds numbers typical of molecular clouds due to the intrinsic or numerical viscosity of any finite-difference or spectral method. However, if the details of behavior at the dissipation scale do not affect the behavior of larger scales, then all that is required is a low enough viscosity to separate the two scales. Incompressible turbulence appears to behave like this (e.g. Lesieur 1997). Resolution studies of energy decay in supersonic compressible turbulence suggest that it may also be true in this case (Mac Low et al. 1998a). The resolution studies we do here also address this question, as increasing the resolution decreases the dissipation scale, which is always close to the zone size.

We use both Lagrangian and Eulerian numerical methods to solve the equations of self-gravitating hydrodynamics in three dimensions (3D) in an attempt to bracket reality by taking advantage of the strengths of each approach. This also gives us some protection against interpreting numerical artifacts as physical effects. The Lagrangian method we use is smoothed particle hydrodynamics (SPH), while the Eulerian method is the astrophysical hydrocode ZEUS. In future work we use this numerical calibration in the interpretation of self-gravitating MHD models computed with ZEUS.

3.1. SPH

SPH is a Lagrangian, particle-based scheme to solve the equations of hydrodynamics. The fluid is represented by an ensemble of particles, each carrying mass, momentum, and thermodynamical properties. Fluid properties at any point are obtained by averaging over a set of neighboring particles. The time evolution of the fluid is represented by the time evolution of the particles, governed by the equation of motion and equations to implement hydrodynamic properties. The technique can therefore be seen as an extension of the pure gravitational N -body system. Excellent overviews of the method, its numerical implementation, and some of its applications are given by the reviews by Benz (1990) and Monaghan (1992). The code used here derives from a version originally developed by Benz (1990). It includes a standard von Neumann-type artificial viscosity (Monaghan & Gingold 1983) with the parameters $\alpha_v = 1$ and $\beta_v = 2$ for the linear and quadratic terms. The system is integrated in time using a second-order Runge-Kutta-Fehlberg scheme, allowing individual time steps for each particle. Furthermore, the smoothing volume over which hydrodynamic quantities are averaged in the code is freely adjustable in space and time such that the number of neighbors for each particle remains approximately fifty.

SPH can resolve very high density contrasts because it increases the particle concentration, and thus the effective spatial resolution, in regions of high density, making it well suited for computing collapse problems. Conversely, it resolves low-density regions poorly. Shock structures tend to be broadened by the averaging kernel in the absence of adaptive techniques. It is also very difficult to include magnetic fields in the algorithm. SPH can be run on the special-purpose hardware device GRAPE (Sugimoto et al. 1990, Ebisuzaki et al. 1993; and also Umemura et al. 1993, Steinmetz 1996), which allows supercomputer-level calculations to be done on a normal workstation. As we concentrate on subregions inside molecular clouds of much larger extent, we use periodic boundary conditions, as implemented by Klessen (1997) on GRAPE.

The correct numerical treatment of gravitational collapse requires the resolution of the local Jeans mass at every stage of the collapse (Bate & Burkert 1997). In the current code, once an object with density beyond the resolution limit of the code has formed in the center of a collapsing gas clump it is replaced by a ‘sink’ particle (Bate, Bonnell, & Price 1995). This particle has a fixed radius on the order of the Jeans length at the threshold density. We set this density to be 10^4 times the average density in the simulation, which roughly corresponds to the maximum resolvable density contrast. The sink particle inherits the combined mass of the replaced SPH particles, as well as their linear and angular momenta. It has the ability to accrete further SPH particles from its infalling gaseous envelope, which are then removed from the computation. Adequately replacing high-density cores and keeping track of their further evolution in a consistent way prevents the time step from becoming prohibitively small. We are thus able to follow the collapse of a large number of cores until the overall gas reservoir becomes exhausted.

3.2. ZEUS-3D

ZEUS-3D is a well-tested, Eulerian, finite-difference code (Stone & Norman 1992, Clarke 1994). It uses second-order van Leer (1977) advection, and resolves shocks using von Neumann artificial viscosity. Self-gravity is implemented via an FFT-solver for Cartesian coordinates. It also includes magnetic fields in the magnetohydrodynamic approximation. For the models discussed here, we use a three-dimensional, periodic, uniform, Cartesian grid. This gives us equal resolution in all regions, and allows us to resolve shocks well everywhere. On the other hand, collapsing regions cannot be followed to scales less than one or two cells.

We must again consider the resolution required for gravitational collapse. For a grid-based simulation, the criterion given by Truelove et al. (1997) holds. Equivalent to the SPH resolution criterion, the mass contained in one grid zone has to be smaller than the local Jeans mass throughout the computation. Applying this criterion strictly would limit our simulations to the very first stages of collapse, as we have not implemented anything like sink particles in ZEUS. We have therefore extended our models beyond the point of

full resolution of the collapse, as we are primarily interested in the formation of collapsed regions, but not their subsequent evolution. Thus, in the ZEUS models, the fixed spatial resolution of the grid implies that strongly collapsed cores have a larger cross-section than appropriate for their mass. In encounters with shock fronts the probability for these cores to get destroyed or lose material is overestimated. Cores simulated with ZEUS are therefore more easily disrupted than they would be physically. SPH, on the other hand, underestimates the disruption probability, because sink particles cannot lose mass or dissolve again once they have formed. The physical result is thus *bracketed* by these two numerical methods (also see § 4).

3.3. Models

We perform our computations using normalized units. The considered volumes are cubes with side $L = 2$, extending from -1 to 1, which are subject to periodic boundary conditions in every direction. The total mass in the box is $M = 1$, therefore the uniform initial density is $\rho_0 = 1/8$. We use an isothermal equation of state, with sound speed $c_s = 0.1$, chosen to set the number of thermal Jeans masses contained in the box to $N_J = 64$. Time is measured in units of the initial global free-fall time of the system.

To generate and maintain turbulent flows we introduce Gaussian velocity fluctuations with power only in a narrow interval $k - 1 \leq |\vec{k}| \leq k$, where $k = L/\lambda_d$ counts the number of driving wave lengths λ_d in the box. This offers a simple approximation to driving by mechanisms that act on that scale. Comparing runs with different k will then give some information on how, for example, turbulence driven by large-scale shearing motions might differ from turbulence driven by low-mass protostars. We set up the initial velocity field as described in Mac Low et al. (1998), with perturbations drawn from a Gaussian random field determined by its power distribution in Fourier space, following the usual procedure. For each three-dimensional wave number \vec{k} we randomly select an amplitude from a Gaussian distribution around unity and a phase between zero and 2π . We then transform the resulting field back into real space to get a velocity component in each zone, and multiply by the amplitude required to get the desired initial root mean square (rms) velocity on the grid. We repeat this for each velocity component independently to get the full velocity field.

To drive the turbulence, we then normalize this fixed pattern to produce a set of perturbations $\delta\vec{v}(x, y, z)$, and at every time step add a velocity field $\delta\vec{v}(x, y, z) = A\delta\vec{v}$ to the velocity \vec{v} . The amplitude A is chosen to maintain constant kinetic energy input rate $\dot{E}_{\text{in}} = \Delta E/\Delta t$. For a compressible flow with a time-dependent density distribution, we maintain a constant energy input rate by solving a quadratic equation in the amplitude A at each time step, as discussed in Mac Low (1999). In dynamical equilibrium, the driving luminosity \dot{E}_{in} equals the rate of turbulent energy dissipation. To estimate the input rate necessary to reach and maintain a certain equilibrium level of the kinetic energy we use equation 7 of Mac Low

(1999). We find that this equation underestimates the driving energy needed to maintain the SPH models at a specific equilibrium kinetic energy by 20–30% for reasons that we do not yet fully understand. Comparisons with other techniques will probably be required to resolve this discrepancy. We drive the SPH models somewhat harder to compensate, as can be seen in table 1 by comparing \dot{E}_{in} for SPH and ZEUS models with equivalent driving wave length k_{drv} and $E_{\text{kin}}^{\text{eq}}$. Dynamical equilibrium is reached typically within one global shock crossing time $t = L/\langle v \rangle$. The equilibrium value is determined to an accuracy of better than 10%. Keeping the energy input unaltered we then switch on self-gravity with gravitational constant $G = 1$, and allow the evolution to proceed. This defines $t = 0$ in our models. Their most important properties are summarized in table 1.

3.4. Scaling

The dynamical behavior of isothermal self-gravitating gas is scale free and depends only on the ratio between potential energy and kinetic energy (including thermal energy). We can scale our models to physical units with a mass scale of the thermal Jeans mass M_{J} given by equation (4), a length scale given by the Jeans length λ_{J} derived from equation (3), and a time scale given by the free-fall time scaled from equation (1)

$$\tau_{\text{ff}} = (0.34 \text{ Myr}) \left(\frac{n}{10^4 \text{ cm}^{-3}} \right)^{-1/2}, \quad (7)$$

where $G = 6.67 \times 10^{-8} \text{ cm}^3 \text{ g}^{-1} \text{ s}^{-2}$, and the number density is taken as $n = \rho/\mu$, with $\mu = 2.36 m_{\text{H}}$. The 120 thermal Jeans masses in our simulation cubes then correspond to

$$M = (413 M_{\odot}) \left(\frac{c_{\text{s}}}{0.2 \text{ km s}^{-1}} \right)^3 \left(\frac{n}{10^4 \text{ cm}^{-3}} \right)^{-1/2}, \quad (8)$$

where a sound speed $c_{\text{s}} = 0.2 \text{ km s}^{-1}$ corresponds to a temperature $T = 11.4 \text{ K}$ with the value of μ we use. Finally we may compute the size of our cube by noting that the Jeans length in our computational units is $\lambda_{\text{J}} = 0.1\sqrt{8\pi} \approx 0.501$, while the size of the cube is $L = 2$, so that in physical units

$$L = (0.89 \text{ pc}) \left(\frac{c_{\text{s}}}{0.2 \text{ km s}^{-1}} \right) \left(\frac{n}{10^4 \text{ cm}^{-3}} \right)^{-1/2}. \quad (9)$$

As an example, let us consider a dark cloud like Taurus with $n(\text{H}_2) \approx 10^2 \text{ cm}^{-3}$, and $c_{\text{s}} \approx 0.2 \text{ km s}^{-1}$. Then our simulation cube holds a mass $M = 4.1 \times 10^3 M_{\odot}$ and has a size $L = 8.9 \text{ pc}$. The time unit (free-fall time scale) is $\tau_{\text{ff}} = 3.4 \text{ Myr}$, and the average *thermal* Jeans mass for the homogeneous distribution follows as $M_{\text{J}} = 65 M_{\odot}$. Another example would be a dense cloud forming massive stars such as the BN region in Orion, with $n(\text{H}_2) \approx 10^5 \text{ cm}^{-3}$ and $c_{\text{s}} \approx 0.2 \text{ km s}^{-1}$. Here the simulated cube holds a mass of $M = 130 M_{\odot}$ and is of size $L = 0.28 \text{ pc}$. The time unit is now $\tau_{\text{ff}} = 0.1 \text{ Myr}$, and the thermal Jeans mass is $M_{\text{J}} = 2.1 M_{\odot}$. (Note again, that in the spherical definition the Jeans mass is smaller by a factor $\pi/6$.)

4. Local vs. Global Collapse

In this section we begin by showing numerical results that suggest that local collapse can occur in turbulent self-gravitating media even if the kinetic energy contained in the system is sufficient to stabilize it on global scales (§ 4.1). The strong shocks ubiquitous in supersonic turbulence compress small regions sufficiently that the turbulence can no longer support them. We then consider what promotes or prevents this process (§ 4.2), and the importance of turbulent collapse in real molecular clouds (§ 4.3).

4.1. Local Collapse in a Globally Stable Region

We compute models with both SPH and ZEUS in which the turbulence is driven at strengths above and below the critical value needed to prevent gravitational collapse according to the analytic predictions of § 2. The models can be characterized by two parameters, the kinetic energy before gravity is turned on, and the typical driving wave number k at which energy is injected (see § 3.3). We define an *effective turbulent Jeans mass* $\langle M_J \rangle_{\text{turb}}$ by substituting $c_s^2 \rightarrow c_s^2 + 1/3 \langle v^2 \rangle$ for the thermal sound speed c_s in equation (4) where we approximate the rms velocity of the flow $\langle v^2 \rangle$ by $2E_{\text{kin}}/M$. We do simulations with $\langle M_J \rangle_{\text{turb}}$ of 0.6, 3.2, and 18.2. These values have to be compared to the total system mass $M \equiv 1$ in order to determine whether global stability is reached. Note that our definition of the Jeans mass uses the mean density in the simulations. This is equivalent to examining the collapse properties of isolated gas cubes. In infinite media (local) density contrasts should be used instead. For this reason, the quoted turbulent Jeans masses are lower limits to the true critical values for support against gravitational collapse. The true stabilizing effect of turbulence on large scales is *stronger* than indicated from merely comparing $\langle M_J \rangle_{\text{turb}}$ with the total mass in the system.

We find that *local* collapse occurs even when the turbulent velocity field carries enough energy to counterbalance gravitational contraction on global scales. This confirms the results of two-dimensional (2D) and low-resolution (64^3) 3D computations with and without magnetic fields by Vázquez-Semadeni et al. (1996). An example of local collapse in a globally supported cloud is given in figure 1. It shows a sequence of 3D density cubes of the SPH model **B2h** which is driven in the wave length interval $3 \leq k \leq 4$ so that the turbulent Jeans mass $\langle M_J \rangle_{\text{turb}} = 3.2$. The first cube shows the system at $t = 0.0$. Hydrodynamic turbulence is fully established but gravity has not yet been included in the computation. (Note again that time is measured in units of the global free-fall time of the system τ_{ff} and the zero-point is set when gravity is switched on). The second cube shows the system at a time $t = 1.1$. Density fluctuations generated by supersonic turbulence in converging and interacting shock fronts that locally exceed the Jeans limit begin to contract. The central regions of these high-density clumps have undergone sufficient gravitational contraction to be identified as

collapsed cores. Numerically, in the SPH code they have been replaced with sink particles. There are altogether twelve cores containing $M_* = 5\%$ of the total gas mass in the system. At $t = 3.9$ the number of dense embedded cores has grown to 46 and they account for 25% of the mass. At $t = 7.1$ roughly 50% of the gas mass is accreted onto 53 dense cores. The first cores form in small groups randomly dispersed throughout the volume. Their velocities directly reflect the turbulent velocity field of the gas they are created from, in which they are still embedded, and from which they continue to accrete. However, as more and more mass accumulates on the cores the gravitational interaction between the cores themselves increasingly determines their dynamical evolution. The core cluster begins to behave more like a collisional N -body system, in which close encounters are dynamically important.

Local collapse in a globally stabilized cloud is not predicted by the analytic models described in Sec. 2. For the parameters of the models presented here, the dispersion relation equation 5 forbids gravitational contraction at any scale. However, this equation was derived under the assumption of incompressibility. The presence of shocks in supersonic turbulence drastically alters the result, as was first noted by Elmegreen (1993) and studied numerically by Vázquez-Semadeni et al. (1996). The density contrast in isothermal shocks scales quadratically with the Mach number, so the shocks driven by supersonic turbulence create density enhancements with $\delta\rho \propto \mathcal{M}^2$, where \mathcal{M} is the *rms* Mach number of the flow. In such fluctuations the local Jeans mass is *decreased* by a factor of \mathcal{M} and therefore the likelihood for gravitational collapse *increased*.

To test this explanation numerically, we designed a test case driven at short enough wave length and high enough power to support even fluctuations with $\delta\rho \propto \mathcal{M}^2$, and ran it with both codes. To ensure sufficient numerical resolution for these models, $\mathcal{B}5$ and $\mathcal{D}5$, we computed a subvolume of mass $M = 0.25$ with reduced sound speed $c_s = 0.05$ driven at wave number $k = 9 - 10$. This is equivalent to an *effective* driving wave number $k = 39 - 40$ on the regular cube ($M = 1$, $c_s = 0.1$). Within $20 \tau_{\text{ff}}$ neither of these models show signs of collapse. All the other globally supported models with less extreme parameters that we computed did form dense cores during the course of their evolution, supporting our hypothesis that local collapse is caused by the density fluctuations resulting from supersonic turbulence.

The two numerical methods that we use are complementary, as discussed in § 3. SPH is a particle based, Lagrangian scheme. It resolves regions of high density well, and the use of sink particles makes it straightforward to define dense cores, but it does not resolve shocks well. Once a collapsing region passes beyond the density threshold and is converted into a sink particle, it cannot be destroyed. It continues to accrete matter from its surroundings and to interact gravitationally with other cores. This *overestimates* the survival probability of collapsing, Jeans-unstable fluctuations. ZEUS, on the other hand, is an Eulerian grid method, well suited for resolving shocks, but worse at modeling gravitational collapse. Due to the fixed grid, it overestimates the volume of collapsed cores, leading to an enhanced cross-section to destructive processes such as tidal interactions between cores, or the pertur-

bations of passing shock fronts. Hence, the probability for core formation and survival in the turbulent environment is *underestimated*. The real behavior of self-gravitating, turbulent gas lies in between, *bracketed* by the two methods which we apply here. Both methods show local collapse occurring in globally stabilized clouds.

Figure 2 illustrates this point by comparing 2D slices through 3D models which are run by the two different codes with similar turbulent driving power spectra at both medium and high resolution. Each slice is centered on the densest core on the grid. (Because we use periodic boundary conditions, we are free to shift the window across the simulated volume in any direction. These boundaries do not introduce artificial perturbations.) Figures 2a and b show the SPH models $\mathcal{B}2$ and $\mathcal{B}2h$ with 50 000 and 200 000 particles, while figures 2c and d show the ZEUS models $\mathcal{D}2$ and $\mathcal{D}2h$ with 128^3 and 256^3 grid zones. We use a new realization of the initial conditions with the same statistical properties for each of these models, so there is no expectation that they will have identical structures, only that they will have similar typical structures. The roundish appearance of structures in the SPH models, especially at lower resolution, stems from the smoothing intrinsic to the SPH algorithm. The Lagrangian nature of the scheme leads to high spatial resolution in high-density regions but degraded resolution in low-density regions where particles are sparse. Conversely, ZEUS does very well at modeling the shock and void structure, especially in the high-resolution model $\mathcal{D}2h$, but the dense collapsed cores are underresolved. The shocks and filaments clearly resolved by the ZEUS model are also present in the SPH model, but tend to be rather smeared out by the lack of resolution in the lower density regions. Nevertheless, *all* the images clearly indicate the presence of strong shocks which sweep up gas into gravitationally collapsing regions.

4.2. Promotion and Prevention of Local Collapse

The total mass and lifetime of a fluctuation determine whether it will actually collapse. Roughly speaking, the lifetime of a clump is determined by the interval between two successive passing shocks: the first creates it, while if the second is strong enough, it disrupts the clump again if it has not already collapsed (Klein, McKee & Colella 1994, Mac Low et al. 1994). If its lifetime is long enough, a Jeans unstable clump can contract to sufficiently high densities to effectively decouple from the ambient gas flow. It then becomes able to survive the encounter with further shock fronts (e.g. Krebs & Hillebrandt 1983), and continues to accrete from the surrounding gas, forming a dense core. The weaker the passing shocks, and the greater the separation between them, the more likely that collapse will occur. Equivalently, weak driving and long typical driving wave lengths enhance collapse. The influence of the driving wave length is enhanced because individual shocks sweep up more mass when the typical wave length is longer, so density enhancements resulting from the interaction of shocked layers will have larger masses, and so are more likely to exceed their local Jeans

limit. Turbulent driving mechanisms that act on large scales will produce large coherent structures (filaments of compressed gas with embedded dense cores) on relatively short time scales compared to small-scale driving even if the total kinetic energy in the system is the same.

We demonstrate the effect of the driving wave length in figure 3, which compares SPH model $\mathcal{B}1h$ with driving wave numbers $k = 1 - 2$ to model $\mathcal{B}3$ driven with $k = 7 - 8$ at a time when sink particles have accreted 5% of the gas mass. (These density cubes can be directly compared with figure 1b, which shows the intermediate case $k = 3 - 4$ at the same evolutionary stage.) Note the difference in the morphology of the density structures. Figure 3a is dominated by *one* large shock front that traverses the volume, which is the sole site of core formation. On the other hand, the density structure in model $\mathcal{B}3$ (figure 3b) is far more homogeneous, without any large-scale structure. Cores form alone, randomly dispersed throughout the volume. This comparison is discussed below in § 6.1.

The influence of driving strength and wave length on local collapse can be examined by measuring the amount of mass accreted onto collapsed regions over time in each model. In the SPH models, this can be computed quite simply by adding up the masses of the sink particles at each time. As ZEUS does not include sink particles, we instead employ a modified version of the CLUMPFIND method (Williams, de Geus, & Blitz 1994; see also appendix 1 in Klessen & Burkert 2000). In this routine, clumps are defined as regions of connected zones whose densities lie above a certain threshold. In order to be able to use CLUMPFIND on models as large as 256^3 zones, we replaced the inefficient clump identification routines with an algorithm based on the dilation operators implemented in IDL. We use two criteria to separate collapsed cores from shock-generated fluctuations. First, we require the average density of those cores to exceed the mean value expected for isothermal shocks, $\rho > \mathcal{M}^2 \rho_0$. Here, \mathcal{M} is the rms Mach number and ρ_0 is the mean density. Second, we count only fluctuations for which the potential energy exceeds the kinetic energy, $E_{\text{kin}}^{\text{core}} < |E_{\text{pot}}^{\text{core}}|$, and which are more massive than the local Jeans mass, $M_* > M_{\text{J}}^{\text{core}}(\rho)$. We use logarithmic density contours instead of linear ones in order to get a wide enough density range so that most detected clumps consist of more than one cell. However, we also accept single high-density cells as cores. These are common at late stages of the evolution, when the envelopes of cores have been removed by further shock interactions and only the collapsed centers remain. In this case the we use the ratio of potential to internal energy as the criterion for collapse.

A figure of merit that we can use to examine the effect of driving strength and wave length is the time $t_{5\%}$ needed to sweep up 5% of the mass into compact cores. Table 1 describes several sequences of models identical except for their driving wave length: the high and medium resolution SPH models $\mathcal{A}1 - \mathcal{A}3$, $\mathcal{B}1 - \mathcal{B}4$ and $\mathcal{C}2$, and the low, medium, and high resolution versions of the ZEUS models $\mathcal{D}1 - \mathcal{D}3$. Comparison of the values of $t_{5\%}$ for these models shows that collapse and accretion occurs more rapidly for models with larger

driving wave length (smaller driving wave numbers and larger typical scales). Comparison of the SPH models with $k = 3 - 4$ shows that stronger driving also delays collapse.

Models run with the same driving strength at different resolutions and with the two different codes can be compared to determine the level of numerical convergence, and the effect of the different algorithms. Comparison of SPH models $\mathcal{B}2l$ to $\mathcal{B}2h$ shows that a change of linear resolution of 2.2 yields a change in $t_{5\%}$ of only 12.5%. Similarly comparison of the 128^3 zone to the 256^3 zone resolution ZEUS models shows better than 10% agreement, except for high wave number driving, where the disagreement is still less than 25%. Comparison of the ZEUS and SPH models with $k = 3 - 4$ driving of the same strength also shows better than 25% quantitative agreement. The 2D cuts through medium and high resolution models with both codes with the same driving wave length ($k = 3 - 4$) and driving strength ($\langle M_J \rangle_{\text{turb}} = 3.2$) presented in figure 2 visually demonstrate the level of morphological agreement. *We emphasize that the qualitative result that local collapse occurs at a rate dependent on the driving wave length and strength is recovered at all resolutions and with both codes.*

A more detailed understanding of how local collapse proceeds comes from examining the full time history of accretion for each model. Figure 4 shows the accretion history for three sets of SPH models. For each set of models, the driving strength is held constant while the effective driving wave length is varied, showing the pronounced effect of the wave length at equal driving strength. At the extreme, if the driving is at wave lengths below the Jeans wave length of the shocked layers local collapse does not occur (model $\mathcal{B}5$). The \mathcal{A} models have lower driving strength than the \mathcal{B} and \mathcal{C} models, demonstrating the effect of driving strength at each driving wave length.

The cessation of strong accretion onto cores occurs long before all gas has been accreted. This appears to be because the time that dense cores spend in shock-compressed, high-density regions decreases with increasing driving wave number and increasing driving strength. In the case of long wave length driving, cores form coherently in high-density regions associated with one or two large shock fronts that can accumulate a considerable fraction of the total mass of the system. The overall accretion rate is high and cores spend sufficient time in this environment to accrete a large fraction of the total mass in the region. Any further mass growth has to occur from chance encounters with other dense regions. In the case of short wave length driving, the network of shocks is tightly knit. Cores form in shock generated clumps of small masses because individual shocks are not able to sweep up much matter. Furthermore, in this rapidly changing environment the time interval between the formation of clumps and their destruction is short. The period during which individual cores are located in high-density regions where they are able to accrete at high rate is short as well. Altogether, the global accretion rates are small and begin to saturate at lower values of M_* as the driving wave length is decreased.

Figure 5 shows the accretion history for the three 256^3 ZEUS models, $\mathcal{D}1h$ to $\mathcal{D}3h$. The fractional core mass M_* in the model with large scale driving ($\mathcal{D}1h$) is strongly affected by

the large shocks that run through the volume. At $t \approx 2.1$, for example, a shock destroys the most massive core, so M_* drops suddenly. Between successive shock passages, the cores recover, so they accrete a substantial mass fraction over the run. Models $\mathcal{D}2h$ and $\mathcal{D}3h$ with $k = 3 - 4$ and $k = 7 - 8$ display a steady mass growth similar to the SPH models. The more frequent shocks in these models reduce the accretion rate by stripping away material from the vicinity of the central high-density zones. These isolated zones do not lose mass from shock encounters, but are subject to numerical clipping, so the measured fraction is, as explained before, a lower limit to the actual accretion fraction. A clear indication of local collapse is once again seen.

To further investigate the influence of numerical resolution, figure 6 compares the time history of accretion for SPH models with varying particle numbers, but identical turbulent Jeans mass $\langle M_J \rangle_{\text{turb}} = 3.2$ and driving wave numbers $3 \leq k \leq 4$ (see table 1). The difference in effective linear resolution (cube root of the particle number) between $\mathcal{B}2\ell$ and $\mathcal{B}2h$ is 2.2. We also had to distinguish the effects of statistical variance from the effects of resolution. To do this, we repeated the intermediate resolution simulation $\mathcal{B}2$ four more times, varying only the random seeds used to generate the Gaussian fields (models $\mathcal{B}2^a$ – $\mathcal{B}2^d$, dashed lines). We actually find stronger variation between the different models at the same resolutions than between models at different resolutions, suggesting that numerical diffusivity doesn’t have as large an effect as the natural statistical variation. This is not surprising given the stochastic nature of turbulent flows. Protostellar cores form in molecular clouds through a sequence of highly probabilistic events. Especially at late times, their mass accretion is strongly influenced by chaotic N -body dynamics (Klessen et al. 1998, Klessen & Burkert 2000). All models agree well at early times when initial local collapse occurs, suggesting that we are well converged on our basic result. At late times, variations between the different models become stronger. These variance effects need to be kept in mind when interpreting the accretion rates of individual models. For the ensemble average at late times we do not expect significant variations at the different numerical resolutions which we study, though our current set of calculations is not large enough to quantify this statement.

Figure 7 shows the time history of accretion for ZEUS models with the same parameters as the SPH models shown in figure 6, and numerical resolution increasing from 64^3 to 256^3 zones. Strong fluctuations in the lower resolution curves are caused by core disruptions due to shocks, which cannot occur in the SPH models as sink particles are never destroyed. The fluctuations decrease with increasing resolution because the cores have smaller cross section in the high resolution models, and are thus less liable to be destroyed by shocks. The high resolution model $\mathcal{D}2h$ shows a well defined accretion behavior and reaches a saturation level at a mass fraction of about 8%, where the local free-fall time of the cores is roughly equal to the time interval between two shock passages. All three models reach this level at least intermittently, suggesting it defines a reasonably firm upper limit for these ZEUS models, and thus a lower limit to the amount of mass that can actually be accreted under these physical conditions, with the SPH models giving an upper limit.

4.3. Application to Molecular Clouds

The *global* star formation efficiency in normal molecular clouds is usually estimated to be of the order of a few per cent. Their life times are typically thought to be a few $\times 10^7$ years which is equivalent to a few tens of their free-fall time τ_{ff} (Blitz & Shu 1980, Blitz 1993, Williams et al. 1999). It would be consistent with these estimations if the mass fraction of protostellar cores in our simulations remained below $M_* = 5\%$ for $10 \tau_{\text{ff}}$. Indeed, as indicated in column 8 of table 1 local collapse can be slowed down considerably in the case of small-scale driving. However, if the hypothesis of rapid molecular cloud evolution is correct (Ballesteros-Paredes et al. 1999, Elmegreen 2000), the constraints on the driving scale and strength are substantially changed. Furthermore, it needs to be noted that the *local* star formation efficiency in molecular clouds can reach very high values. For example, the Trapezium star cluster in Orion is likely to have formed with an efficiency of about 50% (Hillenbrand & Hartmann 1998). In § 6.1 we will argue that this apparent difference between the ‘clustered’ and ‘isolated’ model of star formation can be explained in terms of the properties of the underlying turbulent velocity field of the parental gas.

The energy dissipation scale in molecular clouds should also be considered. It was first shown by Zweibel & Josafatsson (1983) that ambipolar diffusion would be the most important dissipation mechanism in typical molecular clouds with very low ionization fractions $x = \rho_i/\rho_n$, where ρ_i is the density of ions, ρ_n is the density of neutrals, and $\rho = \rho_i + \rho_n$. An ambipolar diffusion strength can be defined as

$$\lambda_{AD} = v_A^2/\nu_{ni}, \quad (10)$$

where $v_A^2 = B^2/4\pi\rho_n$ approximates the effective Alfvén speed for the coupled neutrals and ions if $\rho_n \gg \rho_i$, and $\nu_{ni} = \gamma\rho_i$ is the rate at which each neutral is hit by ions. The coupling constant depends on the cross-section for ion-neutral interaction, and for typical molecular cloud conditions has a value of $\gamma \approx 9.2 \times 10^{13} \text{ cm}^3 \text{ s}^{-1} \text{ g}^{-1}$ (e.g. Smith & Mac Low 1997). Zweibel & Brandenburg (1997) define an ambipolar diffusion Reynolds number as

$$R_{AD} = \tilde{L}\tilde{V}/\lambda_{AD} = \mathcal{M}_A\tilde{L}\nu_{ni}/v_A, \quad (11)$$

which must fall below unity for ambipolar diffusion to be important, where \tilde{L} and \tilde{V} are the characteristic length and velocity scales, and $\mathcal{M}_A = \tilde{V}/v_A$ is the characteristic Alfvén Mach number. In our situation we again can take the rms velocity as typical value for \tilde{V} . By setting $R_{AD} = 1$, we can derive a critical length scale below which ambipolar diffusion is important

$$\tilde{L}_{cr} = \frac{v_A}{\mathcal{M}_A\nu_{ni}} \approx (0.041 \text{ pc}) \frac{B_{10}}{\mathcal{M}_A x_6 n_3^{3/2}}, \quad (12)$$

where the magnetic field strength $B = 10B_{10} \mu G$, the ionization fraction $x = 10^{-6}x_6$, the neutral number density $n_n = 10^3 n_3 \text{ cm}^{-3}$, and we have taken $\rho_n = \mu n_n$, with $\mu = 2.36 m_{\text{H}}$.

We can attempt to compare this value to the numerical dissipation scale by directly computing the ratio of the thermal Jeans length λ_J that we use to scale our models (as discussed in § 3.4) to \tilde{L}_{cr} . We do this by assuming that ionization and magnetic field both depend on the density of the region, following the empirical laws $n_i = 3 \times 10^{-3} \text{ cm}^{-3} (n_n/10^5 \text{ cm}^{-3})^{1/2}$ (e.g. Mouschovias 1991), and $B_{10} \sim 3 n_3^{1/2}$ (e.g. the observational summary of Crutcher 1999). We can then find the interesting result that

$$\frac{\lambda_J}{\tilde{L}_{cr}} = 16.1 \mathcal{M}_A \left(\frac{c_s}{0.2 \text{ km s}^{-1}} \right). \quad (13)$$

Crutcher (1999) suggested that typical values of the Alfvén Mach number \mathcal{M}_A are only slightly above unity. With the value in our simulations $\lambda_J = 0.1\sqrt{8\pi} \approx 0.5$ (cf. §3.4) and noting that our cube has a side length of $L = 2 \approx 4\lambda_J$, this implies that the critical length scale on which ambipolar diffusion becomes important in our model units is $\tilde{L}_{cr} = L/64$. This is comparable to or even slightly greater than the length on which numerical dissipation acts in our highest resolution models. Thus, we can conclude somewhat surprisingly that we may be close to capturing the full dissipation-free range available to real molecular clouds in our models.

5. Fourier Analysis

In this section we discuss the energy distribution on different spatial scales during various stages of the dynamical evolution of the system. We perform a Fourier analysis of the energy, computing the power spectra of kinetic and potential energies. To allow for a direct comparison, all models are analyzed on a Cartesian grid with 128^3 cells. For the SPH models this is done using the kernel smoothing algorithm, while the 256^3 -ZEUS models are simply degraded in resolution. For each cell the potential and kinetic energy content is calculated, and the kinetic energy is further decomposed into its solenoidal (rotational) and compressional parts. These quantities are then all transformed into Fourier space, to find the contribution of different dimensionless wave numbers k , or equivalently, to find the distribution of energy over different spatial scales $\lambda_k = L/k$.

The energy spectrum of fully developed turbulence for small-, medium- and large-scale driving is shown in figure 8. It shows the SPH models (a) $\mathcal{A}1$, (b) $\mathcal{A}2$ and (c) $\mathcal{A}3$ just at the time $t = 0.0$ when gravity is turned on. In each plot the thick solid lines describe the potential energy as a function of wave number k , and the thick long-dashed lines represent the kinetic energy, which can be decomposed into its solenoidal (rotational) and compressional components. They are defined via the velocities by $\vec{\nabla} \cdot \vec{v}_{sol} = 0$ and $\vec{\nabla} \times \vec{v}_{com} = 0$, respectively.

The models $\mathcal{A}1$ and $\mathcal{A}2$, which are driven at long and intermediate wave lengths ($k = 1 - 2$ and $k = 3 - 4$), appear to exhibit an inertial range below the driving scale, i.e. between $0.5 \lesssim \log_{10} k \lesssim 1.5$. Note that, in real clouds, the dissipation scale may lie near the upper

end of this wave number range as discussed in § 4.3. In this interval the energy distribution approximately follows a power law very similar to that predicted by the Kolmogorov (1941) theory ($E_{\text{kin}} \propto k^{-5/3}$). This is understandable given that, in our models, once turbulence is fully established, the solenoidal component of the kinetic energy always dominates over the compressible one, $E_{\text{sol}} > E_{\text{com}}$. For a pure shock dominated flow ($E_{\text{com}} \gg E_{\text{sol}}$) one would expect a power spectrum with slope -2 (Passot et al. 1988). To guide the eye, both slopes are indicated as thin dotted lines in plots (a) to (c). For model $\mathcal{A}3$ the smaller number of available modes between the driving scale $k = 7 - 8$ and the Nyquist frequency does not allow for an unambiguous identification of a turbulent inertial range. The permanent energy input necessary to sustain an equilibrium state of turbulence produces a signature in the energy distribution at the driving wave length. This is most clearly visible in figure 8c.

The system is globally stable against gravitational collapse, as indicated by the fact that for every wave number k the kinetic energy exceeds the potential energy. For comparison we plot in figure 8d the energy distribution of a system without turbulent support. The data are taken from Klessen et al. (1998) and stem from an SPH simulation with 500 000 particles containing 220 thermal Jeans masses and no turbulent velocity field, but otherwise identical physical parameters. The snapshot is taken at $t = 0.2\tau_{\text{ff}}$ after the start of the simulation. This system contracts on *all* scales and forms stars at very high rate within a few free-fall times τ_{ff} . Contrary to the case of hydrodynamic turbulence, the kinetic energy distribution is dominated by compressional modes, especially at small wave numbers. The overall energy budget is determined by the potential energy E_{pot} , which outweighs the kinetic energy E_{kin} on all spatial scales k by about an order of magnitude.

Figure 9 concentrates on model $\mathcal{B}2h$ with $\langle M_{\text{J}} \rangle_{\text{turb}} = 3.2$ and $k = 3 - 4$. It describes the time evolution of the energy distribution. Figure 9a shows the state of fully established turbulence for this model just when gravity is turned on ($t = 0.0$). In the subsequent evolution, local collapse occurs in shock-generated density enhancements where the potential energy dominates over the kinetic energy. This affects the *small* scales first, as seen in the plotted time sequence. As collapse progresses to higher and higher densities, the scale where the potential energy dominates rapidly grows. Once the mass fraction in dense cores has reached about $\sim 3\%$, the potential energy outweighs the kinetic energy on all scales. However, this should not be confused with the signature of global collapse. The power spectrum of the potential energy is constant for all k . It is the Fourier transform of a delta function. Local collapse has produced point-like high-density cores. The overall filling factor of collapsing clumps and cores is very low, so most of the volume is dominated by essentially pure hydrodynamic turbulence. As a consequence, the velocity field on large scales is not modified much (besides a shift to higher energies). On small scales, however, the flow is strongly influenced by the presence of collapsed cores which is noticeable as a flattening of the power spectra at large wave numbers. Despite their small volume filling factor, the cores dominate the overall power spectrum. The solenoidal part of the kinetic energy always dominates over the compressional modes and also the signature of the driving source in the

energy spectrum remains, visible as a ‘bump’ in the kinetic energy spectrum at $k \approx 8$.

To show that the *global* features of our models are insensitive to the numerical method used, in figure 10 we compare the energy spectra of four different simulations with identical physical parameters. Analogously to figure 2, we chose simulations $\mathcal{B}2$, $\mathcal{B}2h$, $\mathcal{D}2$ and $\mathcal{D}2h$ which all have $\langle M_J \rangle_{\text{turb}} = 3.2$ and $k = 3 - 4$. Models $\mathcal{B}2$ and $\mathcal{B}2h$ are SPH simulations with 50 000 and 200 000 particles, while $\mathcal{D}2$ and $\mathcal{D}2h$ were calculated using the ZEUS code with a resolution of 128^3 and 256^3 grid zones, respectively. Figures 10a–d directly compare the different energy components in the four models at $t = 0$, at the stage of fully developed pure hydrodynamic turbulence just before gravity is switched on. The sequence 10e–h does the same after gravity has been switched on and the first collapsed cores have formed at $t_{5\%}$, when the mass accumulated in dense cores is $M_* = 5\%$ of the total mass. This state is identical to the one depicted in figure 2, allowing for direct comparison.

Comparing the spectra of the different models during the stage of pure hydrodynamic turbulence (figures 10a–d) shows excellent agreement between the energy spectra of the different models, suggesting the energy distribution is well converged. Between the scales of energy input (at $k = 3 - 4$) and diffusive energy loss, all the spectra follow the same power law with slope $-5/3$ (analogous to the spectra shown in figure 8). The dissipation scale manifests itself as a drop-off from the power-law at large wave numbers. The inertial range of turbulence is largest in the high-resolution ZEUS model $\mathcal{D}2h$, where it spans about one order of magnitude in k . The high-resolution SPH and medium-resolution ZEUS models $\mathcal{B}2h$ and $\mathcal{D}2$ have inertial ranges nearly as long. The medium-resolution SPH model $\mathcal{B}2$ has the shortest range with $\Delta \log_{10} k \approx 0.5$. At wave numbers above the dissipation scale, our results are converged to better than 10% in the log of energy.

In the presence of self-gravity, the energy spectra are no longer well converged. The actual density contrast reachable in collapsing cores, or to a lesser extent in shock fronts, depends on the numerical resolution and algorithm used (see § 3). The same applies to the potential energy and to the compressional component of the kinetic energy. Figures 10e and h therefore exhibit significant differences between the various models. These differences are much smaller for the solenoidal part of the kinetic energy, which measures rotational motions and is therefore less sensitive to strong density contrasts in small volumes. Variations in the total kinetic energy distribution are mainly due to differences in the compressional modes.

The rapid energy decrease for wave numbers $\log_{10} k > 1.4$ in the grid-based model $\mathcal{D}2$ is due to the fact that these scales approach the grid resolution. A similar decrease would be seen in the other three models if they were sampled at wave numbers all the way up to the effective resolution (grid size for ZEUS or smoothing length for SPH). Remember that all spectra shown here are computed on the same grid with a linear resolution of 128 cells. Despite the fact that the 256^3 ZEUS model $\mathcal{D}2h$ has been resampled and degraded in resolution, large density contrasts still occur on the smallest scales of the resampled grid. The energy spectra therefore remain flat towards the Nyquist wave number. Similarly, the

use of adaptive particle smoothing lengths in SPH allows the resolution of dense cores smaller than the cell size of the 128^3 grid used for the energy sampling. Again, there is no loss of power towards the Nyquist wave number of the spectra. However, high resolution in high density regions is achieved at the cost of low resolution in voids. As low density regions occupy most of the volume, on large scales the SPH simulations tend to have lower energy content than the grid-based models.

Understanding these various effects allows us to understand what questions we can reasonably ask of these simulations. The presence or absence of collapse and the distribution of kinetic energy on large scales are questions for which we can give well-converged answers, but the details of the strength of that collapse still depend on the details of the numerical method and should not be used quantitatively.

6. Implications for Star Formation in Molecular Clouds

In § 4 we have shown that the rate and efficiency of local collapse in turbulent molecular clouds depend on the strength and the effective wave length of the driving energy input. Star formation will follow local collapse (e.g. Vázquez-Semadeni, Canto, & Lizano 1998), so we can use these properties of our turbulence models to try to explain the observed spatial and age distributions of young stars in molecular clouds. We use the spatial and age distributions of sink particles generated in the SPH models with different parameters for this purpose.

6.1. Clustered vs. Isolated Star Formation

Different star formation regions present different distributions of protostars and pre-main sequence stars. In some regions, such as the Taurus molecular cloud, stars form isolated from other stars, scattered throughout the cloud (Mizuno et al. 1995). In other regions, they form in clusters, as in L1630 in Orion (Lada 1992), or even more extremely in starburst regions such as 30 Doradus (Walborn et al. 1999).

From the simulations presented here, it is evident that the *length scale* and *strength* at which energy is inserted into the system determine the structure of the turbulent flow and therefore the locations at which stars are most likely to form. Large-scale driving leads to large coherent shock structures (see e.g. figure 3a). Local collapse occurs predominantly in filaments and layers of shocked gas and is very efficient in converting gas into stars. This leads to what we can identify as ‘clustered’ mode of star formation: stars form in coherent aggregates and clusters. Even more so, this applies to regions of molecular gas that have become decoupled from energy input. As turbulence decays, these regions begin to contract and form dense clusters of stars with very high efficiency on about a free-fall time scale (Klessen et al. 1998, Klessen & Burkert 2000). The same holds for insufficient support,

i.e. for regions where energy input is not strong enough to completely balance gravity. They too will contract to form dense stellar clusters.

The ‘isolated’ mode of star formation occurs in molecular cloud regions that are supported by driving sources that act on *small* scales and in an incoherent or stochastic manner. In this case, individual shock induced density fluctuations form at random locations and evolve more or less independently of each other. The resulting stellar population is widely dispersed throughout the cloud and, as collapsing clumps are exposed to frequent shock interaction, the overall star formation rate is low.

To demonstrate these points, we compare in figure 11 the distribution of sink particles for several different models, projected onto the xy - and xz -planes. As an example of coherent local collapse, we choose model **B1**, where the turbulence is driven strongly at long wave lengths. The flow is dominated by large coherent shocks, so cores form in aggregates associated with the filamentary structure of shock compressed gas (cf. with figure 3). The overall efficiency of converting gas into stars in this ‘clustered’ mode is very high. The upper half of figure 11 compares the model **B1** with model **B3**, which is driven at small scales and results in incoherent collapse behavior. Individual cores form independently of each other at random locations and random times. In this ‘isolated’ mode, cores are widely distributed throughout the entire volume and exhibit considerable age spread.

In the lower half of figure 11 we contrast the large-scale driving model **B1** with a simulation of freely decaying turbulence described by Klessen (2000) that has the same thermal Jeans mass. In decaying turbulence, once the kinetic energy level has decreased sufficiently, all spatial modes of the system contract gravitationally, including the global ones. As in the case of large-scale shock compression, stars form more or less coevally in a very limited volume with high efficiency. Both insufficient turbulent support and the complete loss of it therefore appear to lead to clustered star formation. The Trapezium cluster in Orion may be a good example for the outcome of this mechanism (e.g. Hillenbrand 1997, Hillenbrand & Hartmann 1998). All the projections shown in figure 11 are taken at a stage of the dynamical evolution when the mass accumulated in dense cores is $M_* \approx 20\%$. This occurs at very different times, as noted in the captions, which directly reflects the varying efficiencies of local collapse in these models.

Despite the fact that turbulence that is driven on large scales as well as turbulence that is freely decaying lead to star formation in aggregates and clusters, figure 12 suggests a possible way to distinguish between them by taking the long-term evolution of the resulting clusters into account. Whereas decaying turbulence typically leads to the formation of a bound stellar cluster, the dynamical relaxation of aggregates associated with large-scale coherent shock fronts quite likely results in their complete dispersal. This is illustrated in figure 12, which compares the core distribution in model **B1** and in the decay simulation at $M_* \approx 65\%$, when both systems have already undergone considerable evolution. The cores in model **B1** are completely dispersed throughout the molecular cloud volume. The cluster that

formed during the turbulent decay remains bound with a much longer evaporation time scale. Note, however, that at late stages of the dynamical evolution our isothermal model becomes less appropriate as the feedback effects from newly formed stars are not taken into account. Ionization and outflows from these stars will likely retard or even prevent the accretion of the remaining gas onto the protostars. This limits the validity of our models at very late times.

6.2. The Time Scales of Star Formation

In the previous section we have argued that stellar clusters form predominantly in molecular cloud regions that are insufficiently supported by turbulence or where only large-scale driving is active. In the absence of driving, molecular cloud turbulence decays more quickly than the free-fall time scale (Mac Low 1999). The free-fall time τ_{ff} is thus the typical time scale on which dense stellar clusters will form in the absence of support (Klessen et al. 1998) or in the presence of decaying turbulence (Klessen 2000). Even in the presence of support from large-scale driving, collapse will occur on roughly this time scale, as shown for model $\mathcal{B}1$ in figure 13a. If we assume that once we have identified a dense core it continues to collapse on a very short time scale to build up a stellar object in its center, then this spread relates directly to the star formation time scale. Therefore the age distribution will be roughly τ_{ff} for stellar clusters that form coherently with high star formation efficiency. When scaled to low densities ($n(\text{H}_2) \approx 10^2 \text{ cm}^{-3}$ and $T \approx 10 \text{ K}$) the global free-fall time scale in our models is $\tau_{\text{ff}} = 3.3 \times 10^6$ years. If star forming clouds such as Taurus indeed have ages of order τ_{ff} , as suggested by Ballesteros-Paredes et al. (1999), then the long star formation time scales computed here is quite consistent with the very low star formation efficiencies seen in Taurus (e.g. Leisawitz et al. 1989), as the cloud simply has not had time to form many stars. In the case of high-density regions ($n(\text{H}_2) \approx 10^5 \text{ cm}^{-3}$ and $T \approx 10 \text{ K}$) the dynamical evolution proceeds much faster and the corresponding free-fall time scale drops to $\tau_{\text{ff}} = 1.0 \times 10^5$ years. These values indeed agree well with observational data, e.g. the formation time scale of the Orion Trapezium cluster, which is inferred to stem from gas of density $n(\text{H}_2) \lesssim 10^5 \text{ cm}^{-3}$, is estimated to be less than 10^6 years (Hillenbrand & Hartmann 1998).

The age spread increases with increasing driving wave number k and increasing $\langle M_{\text{J}} \rangle_{\text{turb}}$. Molecular cloud regions supported against global collapse by driving sources that act on small scales host stochastic star formation on much longer time scales and with much lower efficiency. The process is incoherent and the expected stellar age spread therefore larger. Indeed, in figure 13b, which shows the accretion history of selected cores in model $\mathcal{B}2$ with $k = 3 - 4$ (representing more isolated star formation), core formation extends over a longer period. This is even more pronounced in model $\mathcal{B}3$ with $k = 7 - 8$ shown in figure 13c. Note that the real time spread in this model is even larger than suggested by the figure, because

by the time we stopped the simulation the accreted mass fraction was only $M_* = 35\%$. We expect that more cores would form in the subsequent evolution. Models $\mathcal{B}1$ and $\mathcal{B}2$, on the other hand, already reach $M_* \approx 70\%$ in the time interval shown. They each form roughly 50 cores, twice as much as model $\mathcal{B}3$. For a direct comparison, figure 13d plots the distribution of core formation times in each of the three models on the same scale. These long periods of core formation for globally supported clouds appear consistent with the low efficiencies of star-formation in regions of isolated star formation, such as Taurus, even if they are rather young objects with ages of order τ_{ff} .

7. Summary and Conclusions

We have studied the conditions that allow self gravity to cause collapse in a region of supersonic turbulence. We used this study to determine whether interstellar turbulence can support molecular clouds against gravitational collapse, revealing the scales and physical conditions that allow star formation to occur. To perform these studies, we computed numerical simulations of the time evolution of turbulent, self-gravitating, isothermal gas with two different computational schemes: a particle-based, Lagrangian method (SPH); and a second-order, Eulerian, grid-based method (ZEUS). By comparing results from these two different numerical schemes we benefit from the advantages of both methods, and we are furthermore able to estimate the influence of algorithm as well as resolution on our results. We next summarize and discuss our results.

1. Supersonic turbulence strong enough to globally support a molecular cloud against collapse will usually cause *local* collapse. The turbulence establishes a complex network of interacting shocks. The local density enhancements in fluctuations created by converging shock flows can be large enough to become gravitationally unstable and collapse. This occurs if the local Jeans length becomes smaller than the size of the fluctuation. The probability for this to happen, the efficiency of the process, and the rate of continuing accretion onto collapsed cores are strongly dependent on the driving wave length and on the rms velocity of the turbulent flow, and thus on the driving luminosity. Collapse criteria derived from incompressible, self-gravitating turbulence (Chandrasekhar 1951, Bonazzola et al. 1987, 1992, Vázquez-Semadeni & Gazol 1995) indeed determine the *global* or large-scale collapse properties of the medium. However, the occurrence and ubiquity of *local* collapse in shock-generated fluctuations drastically limit the application of these criteria to interpreting the actual behavior of star-forming regions, as *localized* collapse can still occur even if the cloud as a whole is stabilized by turbulence.
2. Fluctuations in turbulent velocity fields are highly *transient*. The random flow that creates local density enhancements can also disperse them. For local collapse to result

in the formation of stars, locally Jeans unstable, shock-generated, density fluctuations must collapse to sufficiently high densities on time scales shorter than the typical time interval between two successive shock passages. Only then are they able to ‘decouple’ from the ambient flow pattern and survive subsequent shock interactions. (If they begin collapse magnetically supercritical, they will remain so for the rest of the collapse.) The shorter the time between shock passages, the less likely these fluctuations are to survive. Hence, keeping the scale of energy input fixed and increasing the driving luminosity leads to a decrease of the star formation efficiency. Local collapse takes longer to occur and the mass accretion rate onto cores is reduced. Similarly, driving on small scales leads to a lower star formation rate than driving on larger scales at the same rms velocity. Quantitatively, our models appear to show that it is possible to prevent 95% of the gas from collapsing into dense cores over ten global free-fall times with strong enough driving on short enough wave lengths. If a physical mechanism for such driving can be found, this could indeed explain the long cloud life times and low star formation rates commonly ascribed to Galactic molecular clouds (Blitz & Shu 1980, Blitz 1993). Conversely, if such driving does not exist, then molecular clouds should be transient objects and the short life times proposed by Ballesteros-Paredes et al. (1999) and Elmegreen (2000) appear more likely.

3. Local collapse can only be halted completely if the turbulent driving mechanism supplies enough energy on scales *smaller* than the Jeans length of the ‘typical’ fluctuation. In supersonic turbulence the typical density contrast is $\delta\rho \propto \mathcal{M}^2$, where \mathcal{M} is the *rms* Mach number of the flow. Thus, the Jeans length is reduced by a factor of \mathcal{M} with respect to the global value. Complete prevention of local collapse requires even stronger and shorter wave length driving, as there will be stochastic turbulent fluctuations with even larger density contrast. However, the time scale for the occurrence of high density fluctuations increases rapidly with $\delta\rho$, so sufficiently strong driving can prevent local collapse for arbitrarily long periods of time. Such strong driving may be rather difficult to arrange in a real molecular cloud, however.

If we assume that stellar driving sources have an effective wave length close to their separation, then the condition that driving acts on scales smaller than the Jeans wave length in ‘typical’ shock generated gas clumps requires the presence of an extraordinarily large number of stars evenly distributed throughout the cloud, with typical separation 0.1 pc in Taurus, or only 350 AU in Orion (taking our fully supported case as an example). This is not observed. Mac Low et al. (1999) show that magnetic fields probably cannot transfer energy efficiently enough to small scales either. Furthermore, ambipolar diffusion may begin to damp turbulent motions at these scales. Unless some other mechanism can force energy onto these small scales, local collapse will occur within globally supported molecular clouds. In addition, very small driving scales seem to be at odds with the observed velocity fields at least in some molecular clouds (e.g. Heyer et al. 1997 for the Cep OB3 cloud).

4. Interstellar clouds driven on large scales or without even global turbulent support very rapidly form stars in clusters. Gas collapses into dense cores within a few free-fall times and the star formation efficiency is more than 50%. On the contrary, in gas that is supported by turbulence driven at small scales, local collapse occurs sporadically over a large time interval, forming isolated stars. The total star formation efficiency before the cloud dissolves due to stellar feedback or external shocks will probably be low. Thus, the strength and nature of the turbulence may be fully sufficient to explain the difference between the observed isolated and clustered modes of star formation.
5. In turbulent flows, it is impossible to predict from the start when and where individual cores form and how they evolve. Firm statistical results can, however, be derived from analyzing large ensembles of cores and from characterizing other global indicators of the dynamical state of the system such as total potential and kinetic energy. In all our models except the ones driven below the fluctuation Jeans scale, gravity eventually begins to dominate over kinetic energy. This first occurs on small scales, indicating the presence of local collapse. As dense collapsed cores form, the power spectrum of the gravitational energy becomes essentially flat. The kinetic energy, on the other hand, appears to follow at intermediate wave numbers a Kolmogorov power spectrum with slope $-5/3$, less steep than the spectrum expected for pure shock flows. The slope remains almost unaltered during the course of the evolution, indicating that a large volume fraction of the system is always well described by pure hydrodynamic turbulence. The spatial extent of collapsing regions (where infall motions dominate over the turbulent flow) is relatively small. This also explains the fact that the solenoidal component of the flow always dominates over the compressional part.

We thank A. Burkert, E. Vázquez-Semadeni, and E. Zweibel for valuable discussions, and P. Padoan for an insightful and exceptionally prompt referee's report. Computations presented here were performed on GRAPE processors at the MPI for Astronomy and at the Sterrewacht Leiden, and on SGI Origin 2000 machines of the Rechenzentrum Garching of the Max-Planck-Gesellschaft, the National Center for Supercomputing Applications (NCSA), and the Hayden Planetarium. ZEUS was used by courtesy of the Laboratory for Computational Astrophysics at the NCSA. This research has made use of NASA's Astrophysics Data System Abstract Service.

REFERENCES

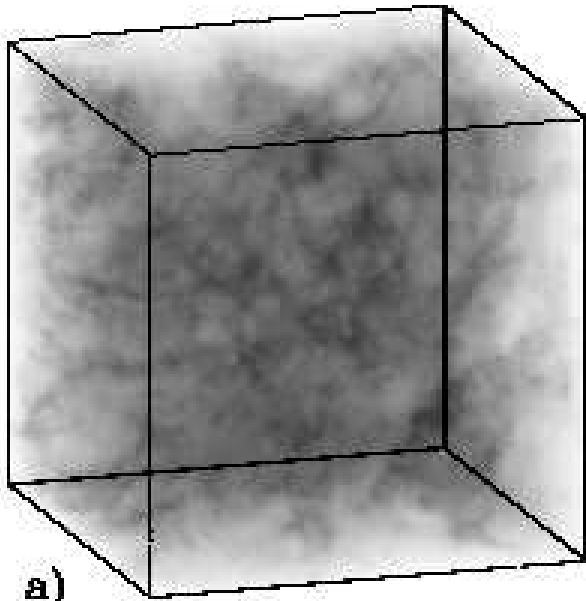
- Benz, W. 1990, in *The Numerical Modelling of Nonlinear Stellar Pulsations*, ed. J. R. Buchler, p. 269, Kluwer Academic Publishers, The Netherlands
- Ballesteros-Paredes, J., Hartmann, L., Vázquez-Semadeni, E. 1999, *ApJ*, 527, 285
- Ballesteros-Paredes, J., Vázquez-Semadeni, E., Scalo, J. 1999, *ApJ*, 515, 286
- Bate, M. R., Burkert, A. 1997, *MNRAS*, 288, 1060
- Bate, M. R., Bonnell, I. A., Price, N. M. 1995, *MNRAS*, 277, 362
- Blitz, L., Shu, F. H. 1980, *ApJ*, 238, 148
- Bonazzola, S., Falgarone, E., Heyvaerts, J., Perault, M., Puget, J. L. 1987, *A&A*, 172, 293
- Bonazzola, S., Perault, M., Puget, J. L., Heyvaerts, J., Falgarone, E., Panis, J. F. 1992, *J. Fluid. Mech.*, 245, 1
- Chandrasekhar, S. 1951. *Proc. R. Soc.*, 210, 26
- Clarke, D. 1994, National Center for Supercomputing Applications Technical Report
- Crutcher, R. M. 1999, *ApJ*, 520, 706
- de Vega, H. J., Sánchez, N. 1999, preprint (hep-th/9903236)
- de Vega, H. J., Sánchez, N., Combes, F. 1996a, *Nature*, 383, 56
- de Vega, H. J., Sánchez, N., Combes, F. 1996b, *Phys. Rev. D*, 54, 6008
- Duerr, R., Imhoff, C. L., & Lada, C. J. 1982, *ApJ*, 261, 135
- Ebisuzaki, T., Makino, J., Fukushige, T., Taiji, M., Sugimoto, D., Ito, T., Okumura, S. K. 1993. *PASJ*, 45, 269
- Elmegreen, B. G. 1993. 419, L29
- Elmegreen, B. G. 2000, *ApJ*, 530 in press (astro-ph/9911172)
- Gammie, C. F., Ostriker, E. C. 1996, *ApJ*, 466, 814
- Heyer, M. H., Schloerb, F. P. 1997, *ApJ*, 475, 173
- Hillenbrand, L. A., Hartmann, L. W. 1998, *ApJ*, 492, 540
- Jeans, J. H. 1902, *Phil. Trans. A.*, 199, 1
- Klein, R. I., McKee, C. F., Colella, P. 1994, *ApJ*, 420, 213
- Klessen, R. S. 1997, *MNRAS*, 292, 11
- Klessen, R. S. 2000, *ApJ*, in press (astro-ph/0001379)
- Klessen, R. S., Burkert, A., Bate, M. R. 1998, *ApJ*, 501, L205
- Klessen, R. S., Burkert, A. 2000, *ApJS*, 128, in press (astro-ph/9904090)
- Kolmogorov, A. N. 1941, *Dokl. Akad. Nauk SSSR*, 30, 9

- Krebs, J., & Hillebrandt, W. 1983, *A&A*, 128, 411
- Lada, E. 1992, *ApJ*, 393, L25
- Larson, R. B. 1981, *MNRAS*, 194, 809
- Leisawitz, D., Bash, F. N., & Thaddeus, P. 1989, *ApJS*, 70, 731
- Léorat, J., Passot, T., Pouquet, A. 1990, *MNRAS*, 243, 293
- Lesieur, M. 1997, *Turbulence in Fluids*, 3rd ed. (Dordrecht: Kluwer), 245
- Mac Low, M.-M. 1999, *ApJ*, 524, 169
- Mac Low, M.-M., McKee, C. F., Klein, R. I., Stone, J. M., and Norman, M. L., 1994, *ApJ*, 433, 757
- Mac Low, M.-M., Klessen, R. S., Burkert, A., Smith, M. D. 1998, *Phys. Rev. Lett.*, 80, 2754
- Mac Low, M.-M., Klessen, R. S., & Heitsch, F. 1999, in *Optical and Infrared Spectroscopy of Circumstellar Matter*, eds. S. Klose, E. Günther, & B. Stecklum, (ASP: San Francisco), in press (astro-ph/9911048)
- Mizuno, A., Onishi, T., Yonekura, Y., Nagahama, T., Ogawa, H., Fukui, Y. 1995, *ApJ*, 445, L161
- Monaghan, J. J. 1992, *ARA&A*, 30, 543
- Monaghan, J. J., Gingold, R. A. 1983. *J. Comp. Phys.*, 52, 135
- Mouschovias, T. Ch. 1991, in *The Physics of Star Formation and Early Stellar Evolution*, eds. C. J. Lada & N. Kylafis (Dordrecht: Kluwer), 61
- Ostriker, E. C., Gammie, C.F., Stone, J. M. 1999, in *Interstellar Turbulence*, eds. J. Franco, A. Carraminana, Cambridge University Press, in press
- Ostriker, E. C., Gammie, C.F., Stone, J. M. 1999, *ApJ*, 513, 259
- Padoan, P., Nordlund, Å. 1999, *ApJ*, 526, 279
- Passot, T., Pouquet, A., Woodward, P. R. 1988, *A&A*, 197, 392
- Porter, D. H., Pouquet, A., Woodward, P. R. 1992, *Theo. & Comp. Fluid Dynamics*, 4, 13
- Porter, D. H., Pouquet, A., Woodward, P. R. 1992, *Phys. Rev. Lett.*, 68, 3156
- Porter, D. H., Pouquet, A., Woodward, P. R. 1994, *Phys. Fluids*, 6, 2133
- Sasao, T. 1973, *PASJ*, 25, 1
- Scalo, J. M. 1985, in *Protostars & Planets II*, eds. D. C. Black & M. S. Matthews (Tucson: U. of Arizona Press), 201
- Smith, M. D., & Mac Low, M.-M. 1997, *A&A*, 326, 801
- Steinmetz, M. 1996, *MNRAS*, 278, 1005

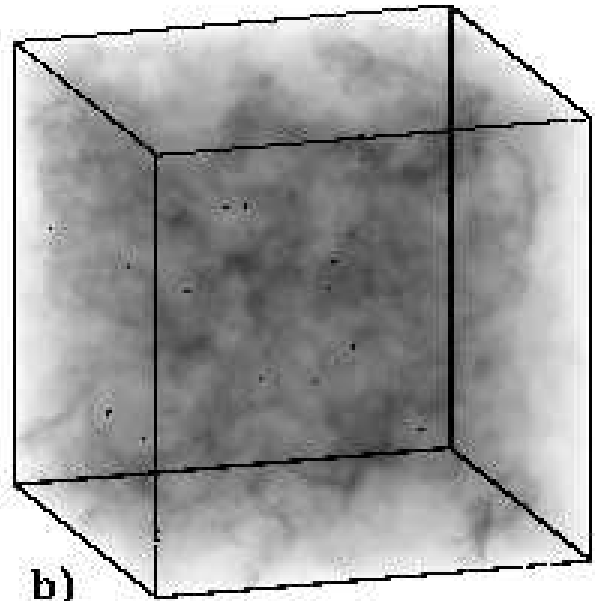
- Sugimoto, D., Chikada, Y., Makino, J., Ito, T., Ebisuzaki, T., Umemura, M. 1990. *Nature*, 345, 33
- Stone, J. M., & Norman, M. L. 1992a, *ApJS*, 80, 753
- Stone, J. M., & Norman, M. L. 1992b, *ApJS*, 80, 791
- Stone, J. M., Ostriker, E. C., Gammie, C. F. 1998, *ApJ*, 508, L99
- Truelove, J. K., Klein, R. I., McKee, C. F. et al. 1997, *ApJ*, 489, L179
- Umemura, M., Fukushige, T., Makino, J., Ebisuzaki, T., Sugimoto, D., Turner, E. L., Loeb, A. 1993, *PASJ*, 45, 311
- van Leer, B. 1977, *J. Comput. Phys.* 23, 276
- Vázquez-Semadeni, E., Gazol, A. 1995, *A&A*, 303, 204
- Vázquez-Semadeni, E., Passot, T., Pouquet, A. 1995, *ApJ*, 441, 702
- Vázquez-Semadeni, E., Passot, T., Pouquet, A. 1996, *ApJ*, 473, 881
- Vázquez-Semadeni, E., Canto, J., & Lizano, S. 1998, *ApJ*, 492, 596
- Vázquez-Semadeni, E., Ballesteros-Paredes, J., Rodríguez, L. F. 1997, *ApJ*, 474, 292
- Von Weizsäcker, C. F. 1943, *Z. Astrophys.* 22, 319
- Von Weizsäcker, C. F. 1951, *ApJ*, 114, 165
- Williams, J. P., De Geus, E., Blitz, L. 1994, *ApJ*, 428, 693
- Williams, J. P., Blitz, L., McKee, C. F. 1999, in *Protostars and Planets IV*, eds. V. Mannings, A. Boss & S. Russell, in press (astro-ph/9902246)
- Walborn, N. R., Barbá, R. H., Brandner, W., Rubio, M., Gredel, E. K., Probst, R. G. 1999, *AJ*, 117, 225
- Zweibel, E. G., & Brandenburg, A. 1997, *ApJ*, 478, 563
- Zweibel, E. G., & Josafatsson, K. 1983, *ApJ*, 270, 511

Name	Method	Resolution	k_{drv}	\dot{E}_{in}	$E_{\text{kin}}^{\text{eq}}$	$\langle M_{\text{J}} \rangle_{\text{turb}}$	$t_{5\%}$
$\mathcal{A}1$	SPH	200 000	1 – 2	0.1	0.15	0.6	0.5
$\mathcal{A}2$	SPH	200 000	3 – 4	0.2	0.15	0.6	0.7
$\mathcal{A}3$	SPH	200 000	7 – 8	0.4	0.15	0.6	2.2
$\mathcal{B}1$	SPH	50 000	1 – 2	0.5	0.5	3.2	0.5
$\mathcal{B}1h$	SPH	200 000	1 – 2	0.5	0.5	3.2	0.4
$\mathcal{B}2\ell$	SPH	20 000	3 – 4	1.0	0.5	3.2	1.6
$\mathcal{B}2$	SPH	50 000	3 – 4	1.0	0.5	3.2	1.5
$\mathcal{B}2h$	SPH	200 000	3 – 4	1.0	0.5	3.2	1.4
$\mathcal{B}3$	SPH	50 000	7 – 8	2.4	0.5	3.2	6.0
$\mathcal{B}4$	SPH	50 000	15 – 16	5.0	0.5	3.2	8.0
$\mathcal{B}5$	SPH	50 000	[39 – 40]	[5.9]	[0.3]	[1.7]	—
$\mathcal{C}2$	SPH	50 000	3 – 4	7.5	2.0	18.2	6.0
$\mathcal{D}1\ell$	ZEUS	64^3	1 – 2	0.4	0.5	3.2	*
$\mathcal{D}2\ell$	ZEUS	64^3	3 – 4	0.8	0.5	3.2	*
$\mathcal{D}3\ell$	ZEUS	64^3	7 – 8	1.6	0.5	3.2	*
$\mathcal{D}1$	ZEUS	128^3	1 – 2	0.4	0.5	3.2	0.4
$\mathcal{D}2$	ZEUS	128^3	3 – 4	0.8	0.5	3.2	1.2
$\mathcal{D}3$	ZEUS	128^3	7 – 8	1.6	0.5	3.2	2.4
$\mathcal{D}5$	ZEUS	128^3	[39 – 40]	[8.3]	[0.5]	[3.2]	—
$\mathcal{D}1h$	ZEUS	256^3	1 – 2	0.4	0.5	3.2	0.4
$\mathcal{D}2h$	ZEUS	256^3	3 – 4	0.8	0.5	3.2	1.2
$\mathcal{D}3h$	ZEUS	256^3	7 – 8	1.6	0.5	3.2	3.1

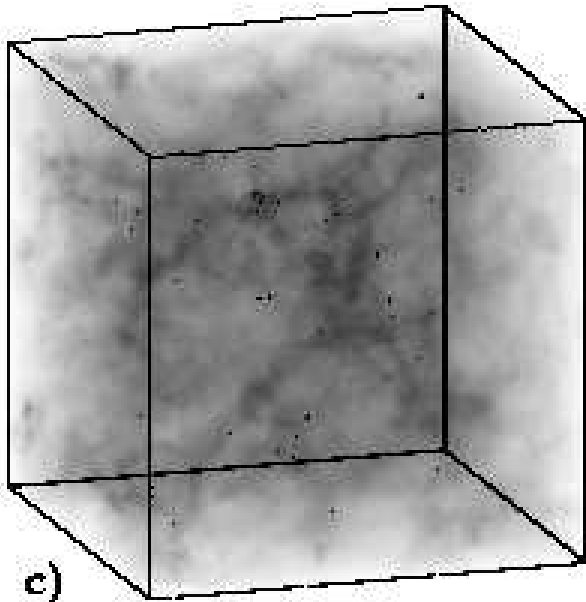
Table 1: Overview of the models. The columns give model name, numerical method, resolution, driving wave lengths k , energy input rate \dot{E}_{in} , equilibrium value of kinetic energy without self-gravity $E_{\text{kin}}^{\text{eq}}$, turbulent Jeans mass $\langle M_{\text{J}} \rangle_{\text{turb}}$, and the time required to reach a core mass fraction $M_* = 5\%$. The resolution is given for SPH as particle number and for ZEUS as number of grid cells. Dashes in the last column indicate that no sign of local collapse was observed within $20\tau_{\text{ff}}$, while stars indicate that the numerical resolution was insufficient for unambiguous identification of collapsed cores. The total mass in the system is $M = 1$. Models $\mathcal{B}5$ and $\mathcal{D}5$ focus on a subvolume with mass $M = 0.25$ and decreased sound speed $c_s = 0.05$. They are driven with $k = 9 - 10$ and $\dot{E}_{\text{in}} = 0.06$. When scaled up to the standard cube this corresponds to the *effective* values given in square brackets. Model $\mathcal{B}2$ has been calculated five times with different random initializations. The additional models are not listed separately, but are called $\mathcal{B}2^a - \mathcal{B}2^d$ in the text.



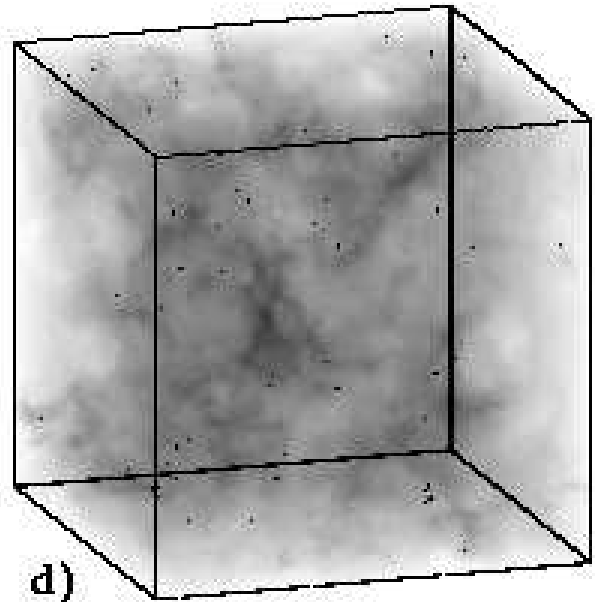
a)
 $t = 0.0$
 $M_* = 0\%$



b)
 $t = 1.1$
 $M_* = 5\%$



c)
 $t = 3.9$
 $M_* = 25\%$



d)
 $t = 7.1$
 $M_* = 50\%$



Fig. 1.— SPH density cubes for model $\mathcal{B}2h$, which is driven in the interval $3 \leq k \leq 4$, shown (a) at the time when gravity is turned on, (b) when the first dense cores are formed and have accreted $M_* = 5\%$ of the mass, (c) when the mass in dense cores is $M_* = 25\%$, and (d) when $M_* = 50\%$. Time is measured in units of the global system free-fall time scale τ_{ff} .

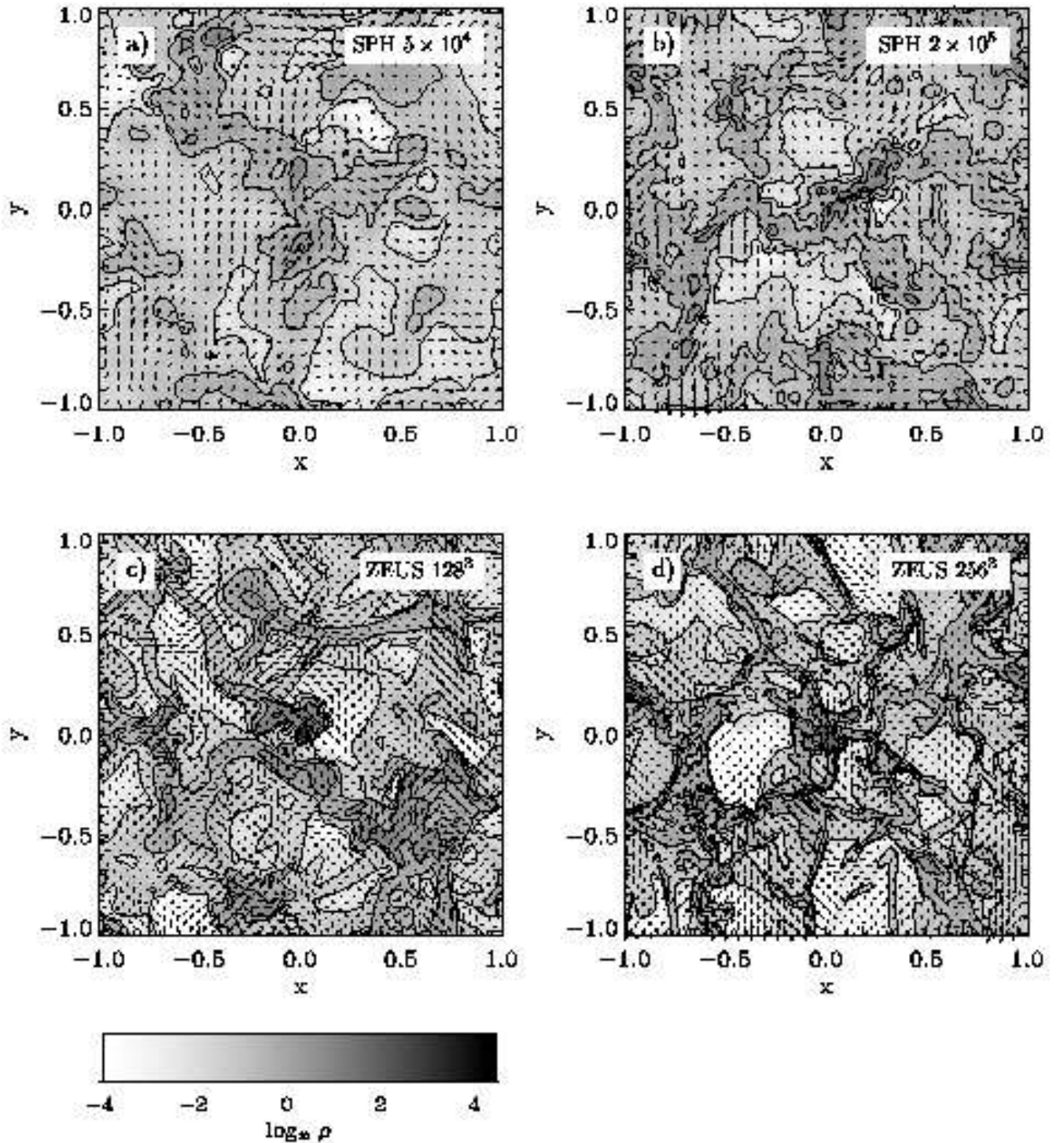


Fig. 2.— Comparison of 2D density slices through 3D models with identical physical parameters ($\langle M_J \rangle_{\text{turb}} = 3.2$ and $k = 3 - 4$) computed with different numerical methods and resolution: SPH models (a) $\mathcal{B}2$ and (b) $\mathcal{B}2h$ with 50 000 and 200 000 particles, and ZEUS models (c) $\mathcal{D}2$ and (d) $\mathcal{D}2h$ with 128^3 and 256^3 grid cells. For further details see table 1. To allow for comparison, the time is chosen such that the mass accreted onto dense cores is $M_* = 5\%$. Density is scaled logarithmically with the separation of contour levels being one decade. Each cut is centered on the density maximum in the simulation. In SPH, the density distribution has been interpolated onto a uniform grid using kernel smoothing. The arrows indicate the velocity components *in* the plane of section.

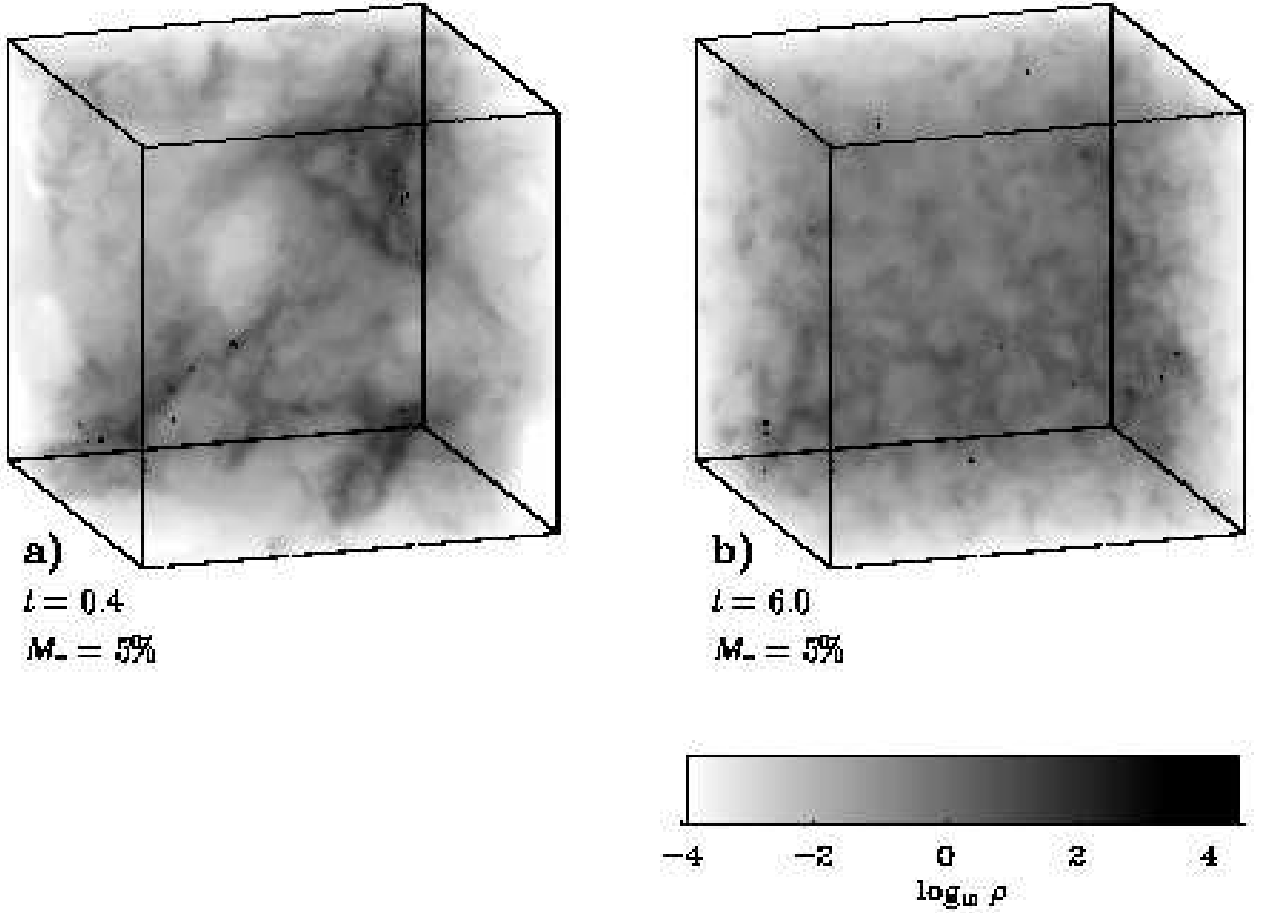


Fig. 3.— Density cubes for models (a) $\mathcal{B}1h$ ($k = 1 - 2$) and (b) $\mathcal{B}3$ ($k = 7 - 8$) at dynamical stages where the core mass fraction is $M_* = 5\%$. Compare these figures with figure 1b. Together they show the influence of different driving wave lengths for otherwise identical physical parameters. Note the different visual appearance of the systems and the different times at which $M_* = 5\%$ is reached.

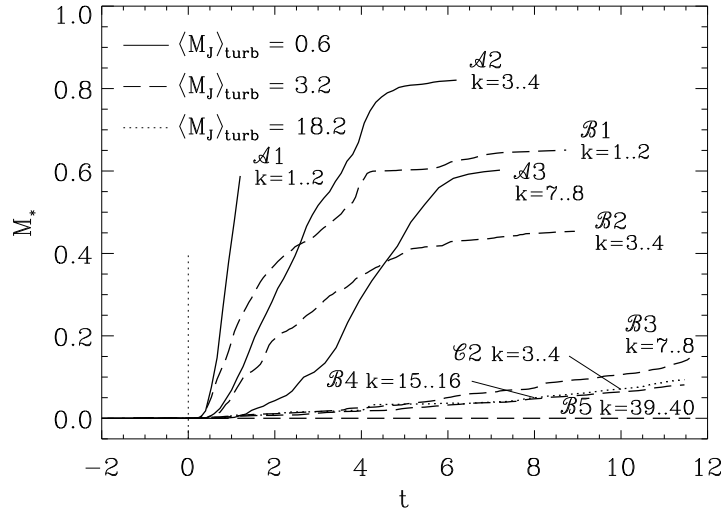


Fig. 4.— Fraction of mass M_* in dense cores as function of time. All models are computed using SPH with sink particles replacing dense, collapsed cores. The different models are indicated in the figure, details can be found in table 1. The figure shows how the efficiency of local collapse depends on the scale and strength of turbulent driving.

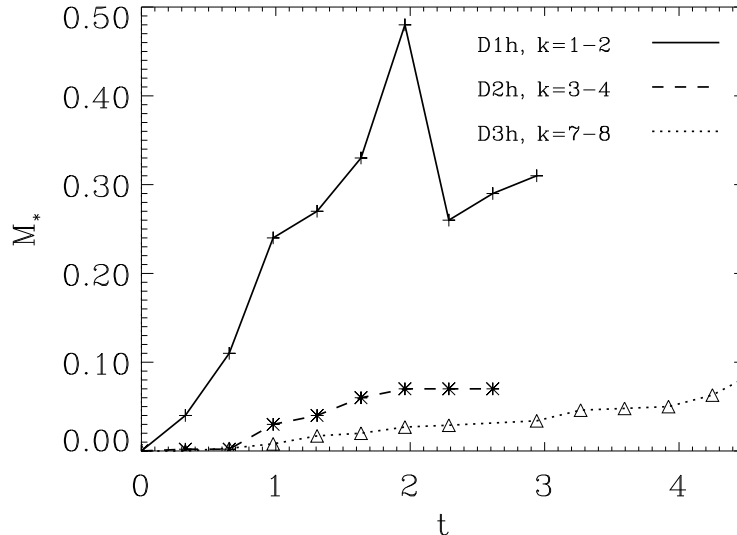


Fig. 5.— Mass fraction M_* in dense cores as function of time for the three 256^3 ZEUS models driven with $k = 1 - 2$ (solid, crosses), $k = 3 - 4$ (dashed, stars) and $k = 7 - 8$ (dotted, triangles). M_* is the sum of all cores found by CLUMPFIND as discussed in the text. Note that the method identifies cores only after gravity is turned on, i.e. for $t > 0.0$.

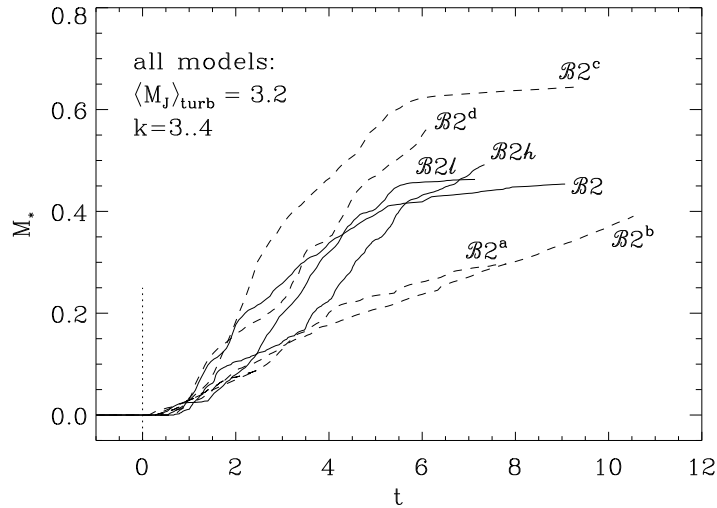


Fig. 6.— Study of resolution and statistical variation of the core mass fraction M_* over time for SPH models with turbulent Jeans mass $\langle M_J \rangle_{\text{turb}} = 3.2$ and $k = 3 - 4$. The low-resolution model $\mathcal{B}2\ell$ has 20 000 particles, for medium-resolution model $\mathcal{B}2$ this number is 50 000, and for the high-resolution model $\mathcal{B}2h$ it is 200 000. Model $\mathcal{B}2$ has been repeated four times with different realizations of the driving field. The alternative models $\mathcal{B}2^a$ to $\mathcal{B}2^d$ are indicated by dotted lines. Note the large variance effect.

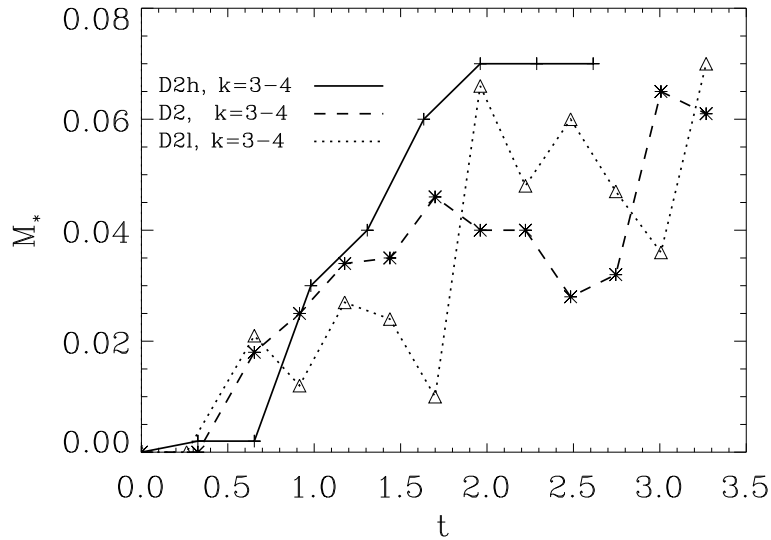


Fig. 7.— Resolution study of core mass fraction M_* as function of time for ZEUS models with turbulent Jeans mass $\langle M_J \rangle_{\text{turb}} = 3.2$ and driving wave number $k = 3 - 4$. The models have resolutions of 64^3 (dotted), 128^3 (dashed), and 256^3 cells (solid). M_* is computed using CLUMPFIND as discussed in the text.

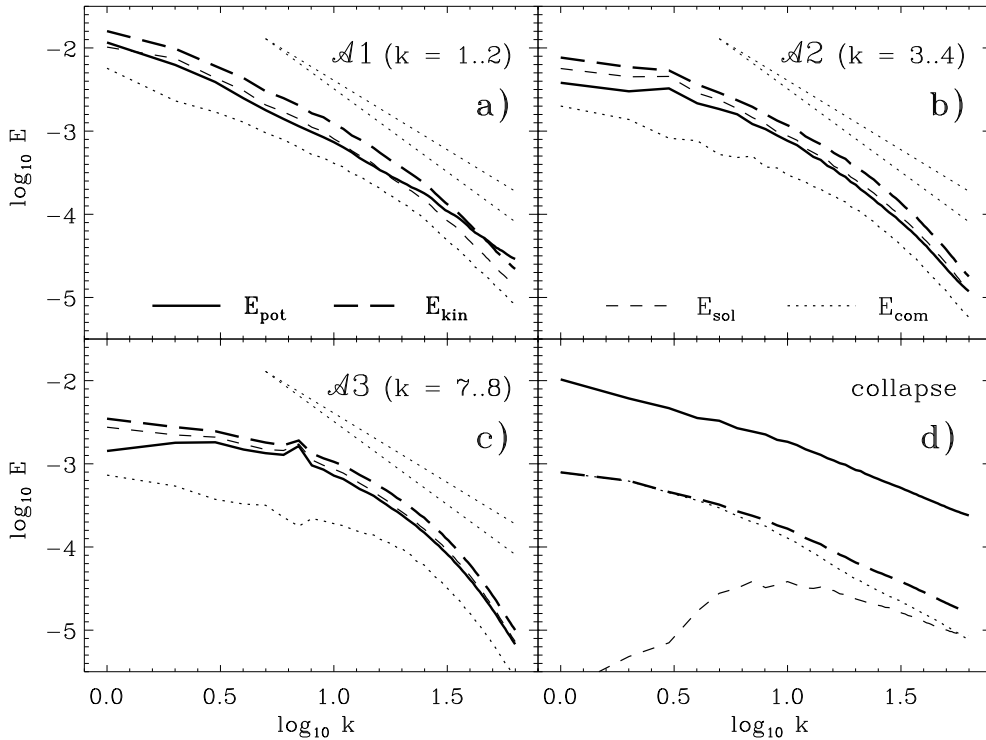


Fig. 8.— Energy as function of wave number k for models with different driving scale: (a) $\mathcal{A}1$ with $k = 1 - 2$, (b) $\mathcal{A}2$ with $k = 3 - 4$ and (c) $\mathcal{A}3$ with $k = 7 - 8$. The simulations are studied at $t = 0.0$, when the hydrodynamic turbulence is fully developed, immediately after gravity is included. The plots show potential energy E_{pot} (thick solid lines), kinetic energy E_{kin} (thick long-dashed lines), its solenoidal component E_{sol} (short-dashed lines) and its compressional component E_{com} (dotted lines). The thin dotted lines indicate the slope $-5/3$ expected from the Kolmogorov (1941) theory and the slope -2 expected for velocity discontinuities associated with shocks. For comparison, plot (d) shows a strongly self-gravitating model that completely lacks turbulent support and therefore contracts on all scales (data from Klessen et al. 1998). The energy spectra are computed on a 128^3 grid onto which the SPH particle distribution has been assigned using the kernel smoothing procedure.

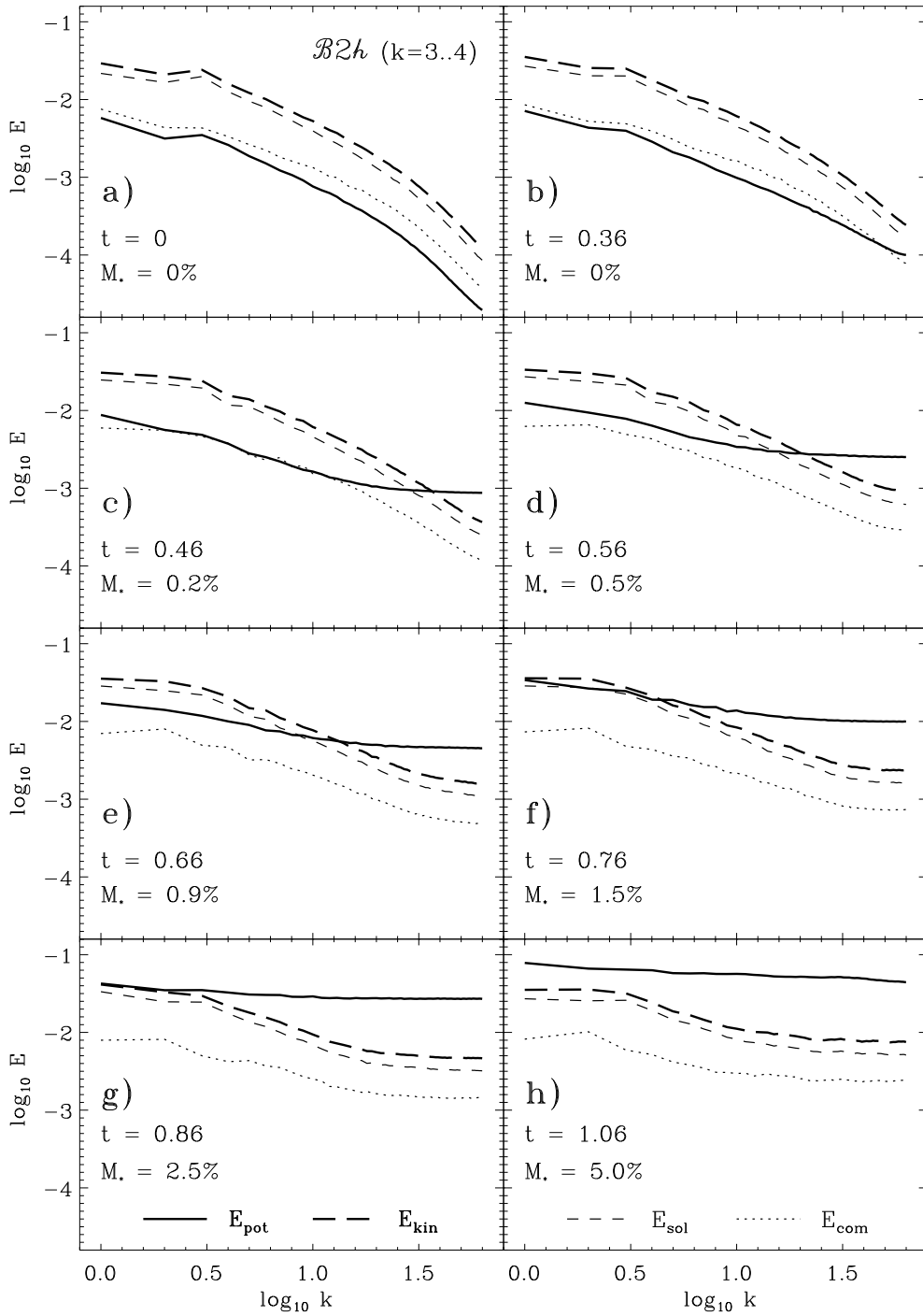


Fig. 9.— Fourier analysis of the high-resolution model $\mathcal{B}2h$ ($\langle M_J \rangle_{\text{turb}} = 3.2$ and $k = 3 - 4$) at different stages of its dynamical evolution indicated on each plot. Notation and scaling are the same as in figure 8. Again, the SPH model is sampled on a 128^3 mesh.

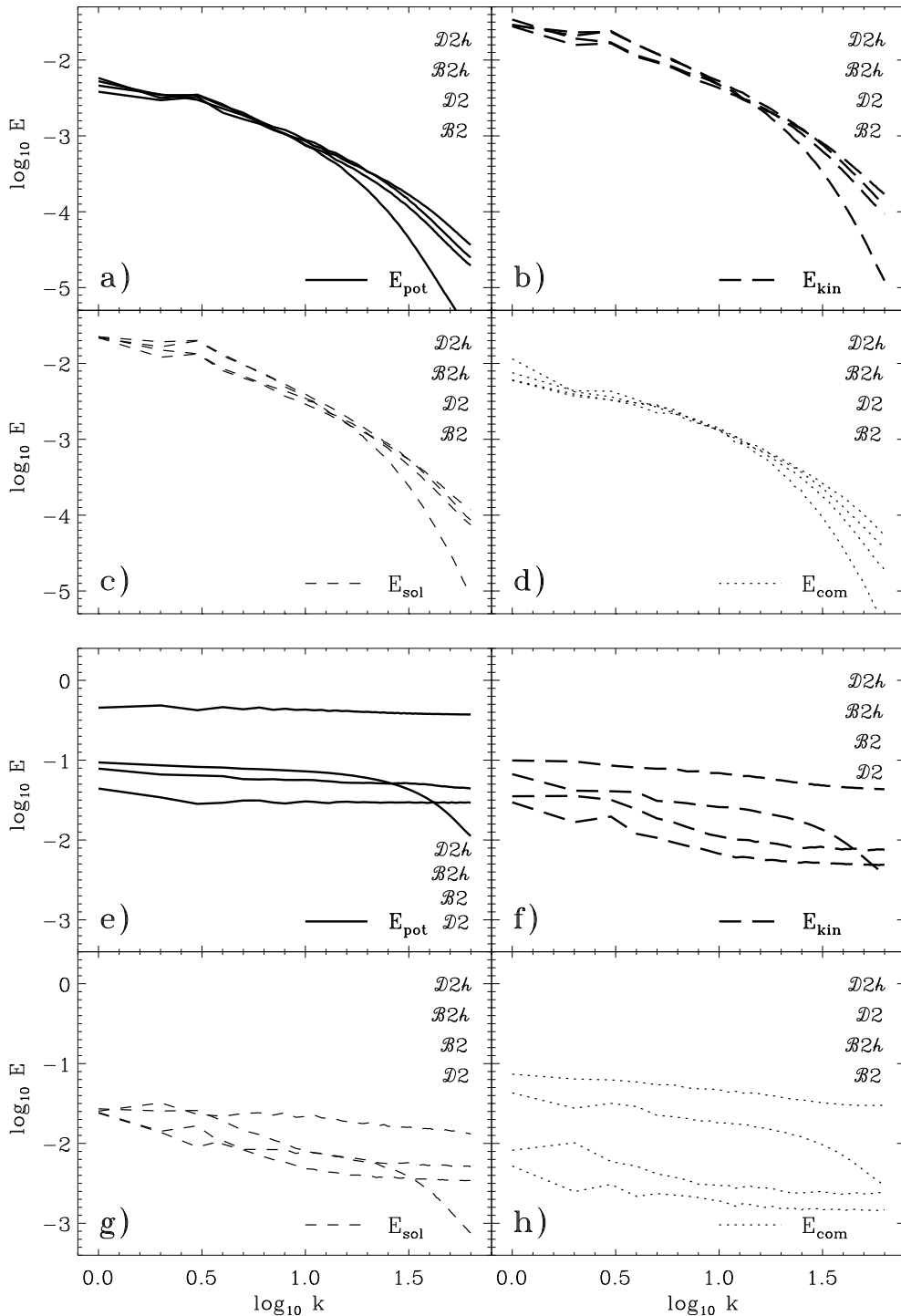


Fig. 10.— Wave mode comparison between four models with identical physical parameters ($\langle M_J \rangle_{\text{turb}} = 3.2$ and $k = 3 - 4$) computed with different numerical methods and resolution: SPH models $\mathcal{B}2$ and $\mathcal{B}2h$ with 50 000 and 200 000 particles, and ZEUS models $\mathcal{D}2$ and $\mathcal{D}2h$ with 128^3 and 256^3 grid cells. To enable direct comparison, equivalent energy components of all four models are plotted in each panel. The upper half (a – d) of the figure shows the energy distribution of a state of fully developed hydrodynamic turbulence without gravity. The lower half (e – h) depicts the system after gravity is included, when $M_* = 5\%$ of the total mass is collapsed onto dense cores. Again, all spectra are computed on a grid with

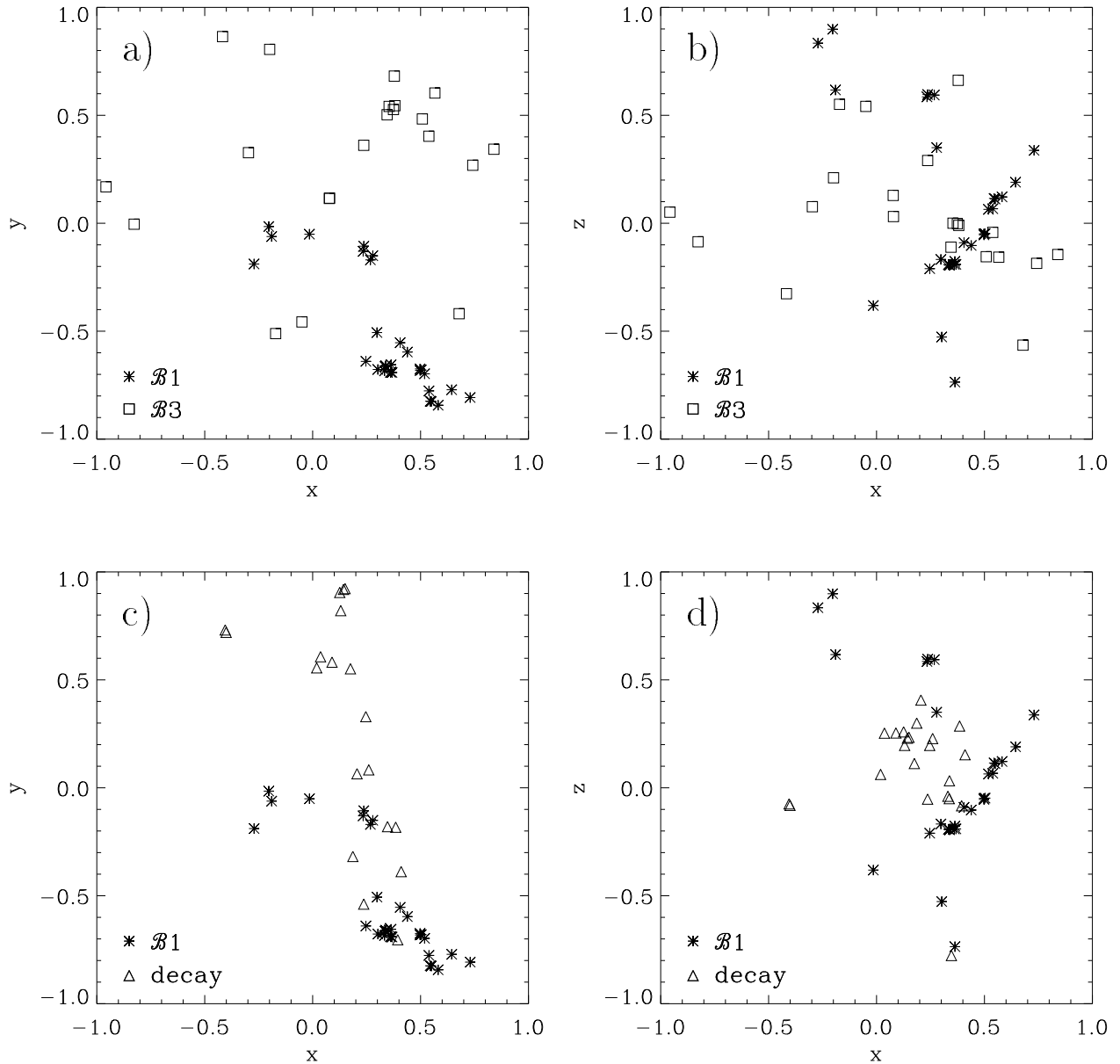


Fig. 11.— Comparison of core locations between two globally stable models with different driving wave length ($\mathcal{B}1$ with $k = 1 - 2$ and $\mathcal{B}3$ with $k = 7 - 8$) projected into (a) the xy -plane and into (b) the xz -plane. Plots (c) and (d) show the core locations for model $\mathcal{B}1$ now contrasted with a simulation of decaying turbulence from Klessen (1999). The snapshots are selected such that the mass accumulated in dense cores is $M_* \lesssim 20\%$. Note the different times needed for the different models to reach this point. For model $\mathcal{B}1$ data are taken at $t = 1.1$, for $\mathcal{B}3$ at $t = 12.3$. The simulation of freely decaying turbulence is shown at $t = 1.1$. All times are normalized to the global free-fall time scale of the system.

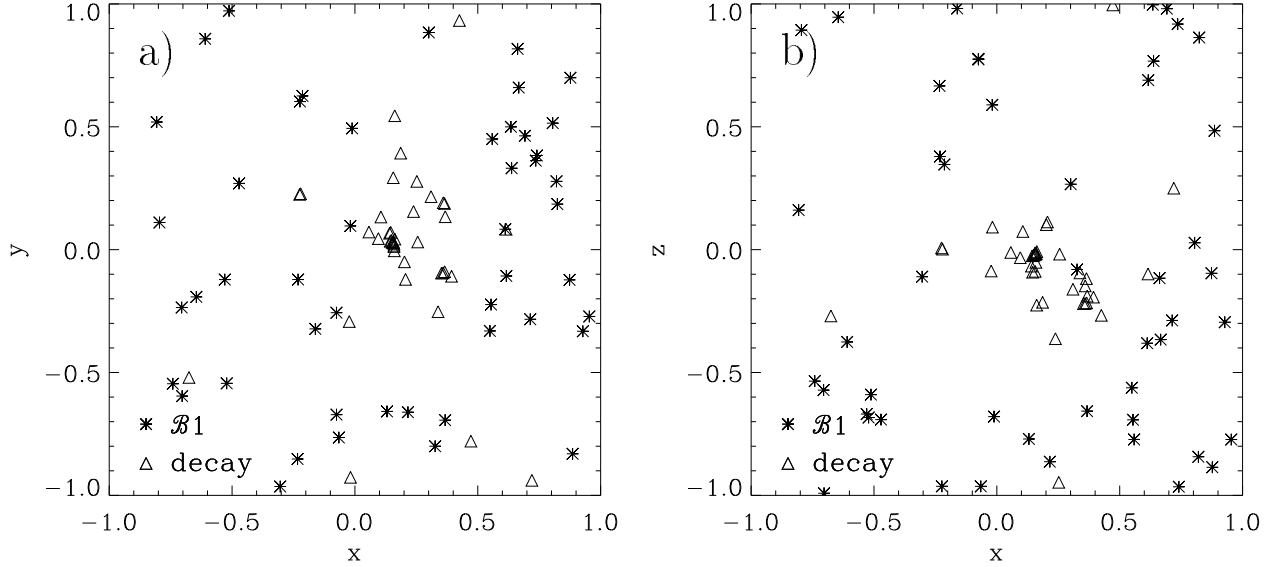


Fig. 12.— Core positions for model $\mathcal{B}1$ ($k = 1 - 2$) and the decay model when the core mass fraction is $M_* \approx 65\%$, projected into (a) the xy -plane and (b) the xz -plane (cf. figure 11c & d). For $\mathcal{B}1$ the time is $t = 8.7$ and for decay model $t = 2.1$. Whereas the cluster in $\mathcal{B}1$ is completely dissolved and the stars are widely dispersed throughout the computational volume, the core cluster in the decay simulation remains bound.

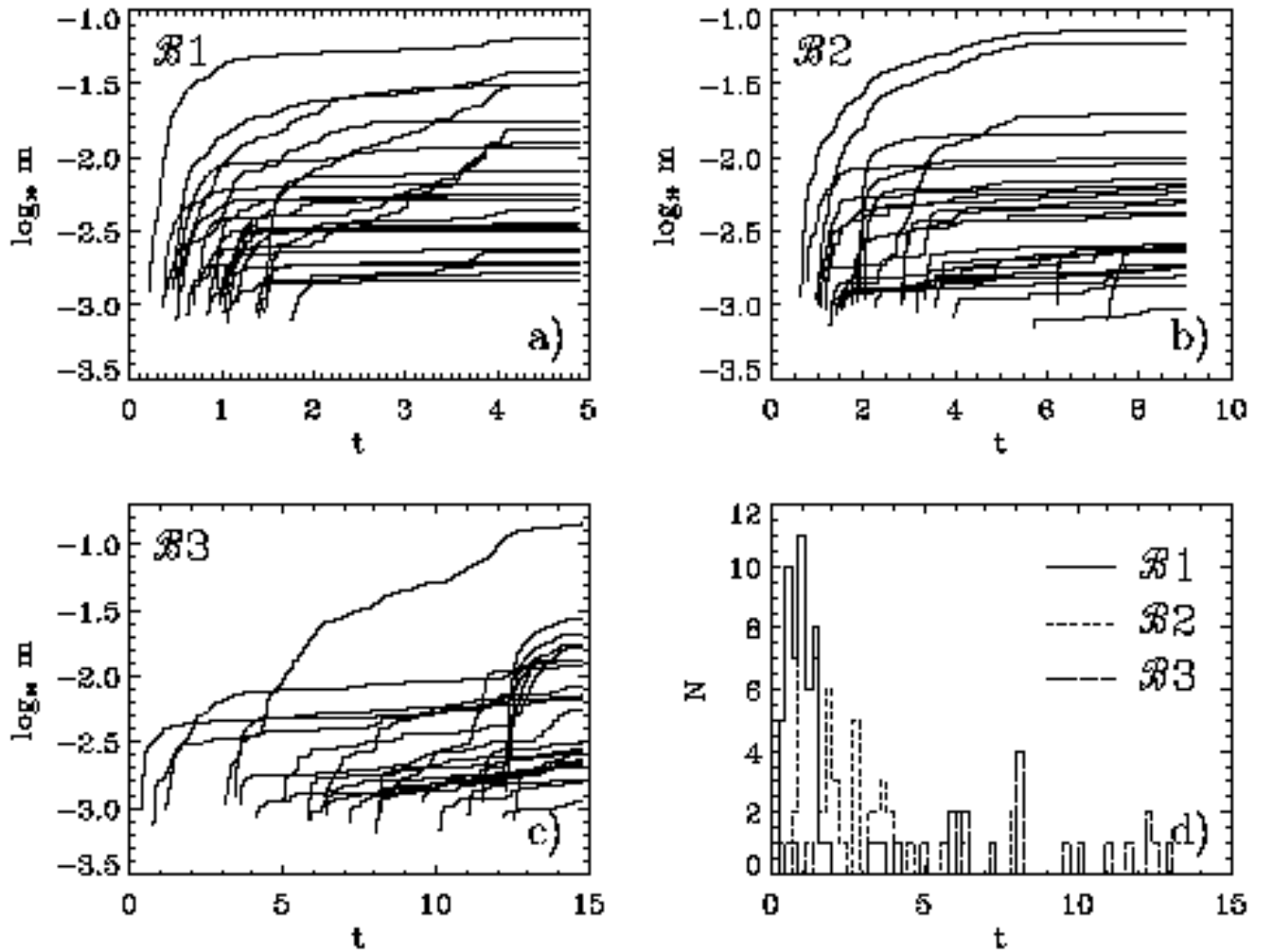


Fig. 13.— Core masses as function of time in SPH models (a) $\mathcal{B}1$ with $k = 1 - 2$ driving, (b) $\mathcal{B}2$ with $k = 3 - 4$ driving, and (c) $\mathcal{B}3$ with $k = 7 - 8$ driving. The curves represent the formation and accretion histories of individual cores. For the sake of clarity, only every other core is shown in (a) and (b), whereas in (c) the evolution of every single core is plotted. Time is given in units of the global free-fall time τ_{ff} . Note the different time scale in each plot. In the depicted time interval models $\mathcal{B}1$ and $\mathcal{B}2$ reach a core mass fraction $M_* = 70\%$, and both form roughly 50 cores. Model $\mathcal{B}3$ reaches $M_* = 35\%$ and forms only 25 cores. Figure (d) compares the distributions of formation times. The age spread increases with decreasing driving scale showing that clustered core formation should lead to a coeval stellar population, whereas a distributed stellar population should exhibit considerable age spread.